Measurement of iodine species and sulfuric acid using bromide chemical ionization mass spectrometers

Mingyi Wang[1,2*], Xu-Cheng He[3*#], Henning Finkenzeller[4], Siddharth Iyer[3], Dexian Chen[1,5], Jiali Shen[3], Mario Simon[6], Victoria Hofbauer[1,2], Jasper Kirkby[6,7], Joachim Curtius[6], Norbert Maier[8], Theo Kurtén[3,8], Douglas R. Worsnop[3,9], Markku Kulmala[3,10,11,12], Matti Rissanen[3,13], Rainer Volkamer[4], Yee Jun Tham[~~3~~14,3#], Neil M. Donahue[1,2,5,1~~5~~4], and Mikko Sipilä[3]

[1]Center for Atmospheric Particle Studies, Carnegie Mellon University, Pittsburgh, PA, 15213, USA
[2]Department of Chemistry, Carnegie Mellon University, Pittsburgh, PA, 15213, USA
[3]Institute for Atmospheric and Earth System Research (INAR), University of Helsinki, 00014 Helsinki, Finland
[4]Department of Chemistry & CIRES, University of Colorado Boulder, Boulder, CO 80309, USA
[5]Department of Chemical Engineering, Carnegie Mellon University, Pittsburgh, PA, 15213, USA
[6]Institute for Atmospheric and Environmental Sciences, Goethe University Frankfurt, 60438 Frankfurt am Main, Germany
[7]CERN, the European Organization for Nuclear Research, CH-1211 Geneve 23, Switzerland
[8]Department of Chemistry, University of Helsinki, 00014 Helsinki, Finland
[9]Aerodyne Research, Inc., Billerica, MA, 01821, USA
[10]Helsinki Institute of Physics, P.O. Box 64 (Gustaf Hallstromin katu 2), FI-00014 University of Helsinki, Finland
[11]Joint International Research Laboratory of Atmospheric and Earth System Sciences, Nanjing University, Nanjing, China
[12]Aerosol and Haze Laboratory, Beijing Advanced Innovation Center for Soft Matter Science and Engineering, Beijing University of Chemical Technology, Beijing, China
[13]Aerosol Physics Laboratory, Physics Unit, Faculty of Engineering and Natural Sciences, Tampere University, Tampere, Finland
[14]School of Marine Sciences, Sun Yat-sen University, Zhuhai 519082, China
[15~~4~~]Department of Engineering and Public Policy, Carnegie Mellon University, Pittsburgh, PA, 15213, USA
[*]These authors contributed equally to this work

[#]*Correspondence to*:
Xu-Cheng He (xucheng.he@helsinki.fi) and Yee Jun Tham (thamyj@mail.sysu.edu.cn ~~yee.tham@helsinki.fi~~).

Abstract. Iodine species are important in the marine atmosphere for oxidation and new-particle formation. Understanding iodine chemistry and iodine new-particle formation requires high time resolution, high sensitivity, and simultaneous measurements of many iodine species. Here, we describe the application of bromide chemical ionization mass spectrometers (Br-CIMS) to this task. During the iodine ~~new-particle formation~~oxidation experiments in the Cosmics Leaving OUtdoor Droplets (CLOUD) chamber, we have measured gas-phase iodine species and sulfuric acid using two Br-CIMS, one coupled to a Multi-scheme chemical IONization inlet (Br-MION-CIMS) and the other to a Filter Inlet for Gasses and AEROsols inlet (Br-FIGAERO-CIMS). From offline calibrations and inter-comparisons with other instruments attached to the CLOUD chamber, we have quantified the sensitivities of the Br-MION-CIMS to HOI, I_2, and H_2SO_4 and obtain detection limits of 5.8×10^6, 3.8~~6.3~~$\times10^5$, and 2.0×10^5 molec cm^{-3}, respectively, for a 2-min integration time. From binding energy calculations, we estimate the detection limit for HIO_3 to be 1.2×10^5 molec cm^{-3}, based on an assumption of maximum sensitivity. Detection limits in the Br-FIGAERO-CIMS are around one order of magnitude higher than those in the Br-MION-CIMS; for example, the detection limits for HOI and HIO_3 are 3.3×10^7 and 5.1×10^6 molec cm^{-3}, respectively. Our comparisons of the performance of the MION inlet and the

46 FIGAERO inlet show that bromide chemical ionization mass spectrometers using either atmospheric pressure or
47 reduced pressure interfaces are well-matched to measuring iodine species and sulfuric acid in marine environments.
48
49 **1 Introduction**
50 Reactive iodine species are released into the atmosphere mainly by biological processes in marine environments (i.e.
51 from macro- and micro-algae) (McFiggans et al., 2004), O_3 deposition on the sea surface (Carpenter et al., 2013), as
52 well as from the sea ice (Spolaor et al., 2013) and snowpack in the polar region (Raso et al., 2017). Once emitted,
53 iodine species can modify atmospheric oxidative capacity via a chain of catalytic reactions with O_3 that form iodine
54 oxides, leading to about 20–28 % of O_3 loss in the marine boundary layer (Prados-Roman et al., 2015; Sherwen et al.,
55 2016). Through convection, reactive iodine species can be transported from the lower troposphere to the upper
56 troposphere-lower stratosphere, causing one third of the iodine-induced ozone loss in the upper troposphere-lower
57 stratosphere (Koenig et al., 2020). Another important effect of iodine species is their contribution to atmospheric new-
58 particle formation. O'Dowd et al. (O'Dowd et al., 2002) showed that particles are produced from condensable iodine-
59 containing vapours at a costal location (Mace Head in Ireland). Recent studies have demonstrated that iodine oxoacids
60 (iodous acid, HIO_2 and iodic acid, iodic acid (HIO_3) dominates the charged iodine cluster formation processes (He et
61 al., 2021a, 2021b), and drives the bursts of freshly-formed particles in coastal regions (Sipilä et al., 2016). This process
62 thereby may enhance cloud condensation nuclei formation, affecting climate both directly and indirectly (Saiz-Lopez
63 et al., 2012; Simpson et al., 2015).
64
65 Understanding iodine chemistry and iodine driven new-particle formation requires high time resolution, high
66 sensitivity, and simultaneous measurements of iodine species. However, this has been a long-standing challenge due
67 to their low abundance and short atmospheric lifetimes. Previous studies have achieved detection of relatively more
68 abundant molecular iodine (I_2), iodine monoxide (IO), and iodine dioxide (OIO) via optical spectroscopy, such as
69 differential optical absorption (Leigh et al., 2010), cavity ring-down (Bitter et al., 2005), cavity enhanced absorption
70 (Vaughan et al., 2008), laser-induced fluorescence (Dillon et al., 2006), and resonance fluorescence (Gómez Martín
71 et al., 2011). The spectroscopic techniques are invaluable; however, their very specificity limits them to the detection
72 of a few iodine compounds, and they are less sensitive to other iodine species that have congested or broad absorption
73 cross sectionsfeatures, such as hypoiodous acid (HOI) and iodic acid (HIO_3).
74
75 Another commonly used technique is mass spectrometry; it has a fast response time and a low detection limit, but
76 extra calibration efforts are needed for the quantification of the detection sensitivity. For example, photoionization
77 (Gómez Martín et al., 2013) and chemical ionization mass spectrometry (CIMS) have been employed to detect a suite
78 of halogen species. Reagent ions used with CIMS include: SF_5^- for HCl and $ClONO_2$ (Marcy et al., 2004); iodide (I^-)
79 for atmospheric chlorine and bromine species such as $ClNO_2$, Cl_2, ClO, BrO, and BrCl (Kercher et al., 2009; Lee et
80 al., 2018; Tham et al., 2016); superoxide (O_2^-) for molecular iodine (I_2) (Finley and Saltzman, 2008); and both nitrate
81 (NO_3^-) (Sipilä et al., 2016) and protonated water (H_3O^+) (Pfeifer et al., 2020) for HIO_3. The nitrate-CIMS and H_3O^+-

CIMS suffer from the limited analyte affinity to the reagent ions. The iodide-CIMS can effectively measure chlorine and bromine species, but it is not suitable to detect iodine species due to the ambiguity in peak identification.

The bBromide ion (Br⁻) exhibits an affinity to a wide spectrum of iodine containing species. Br-CIMS has been routinely used to measure chlorine species (Lawler et al., 2011), HO_2 radicals (Sanchez et al., 2016), organic vapors and sulfuric acid (Rissanen et al., 2019), and nitric acid (Wang et al., 2020). Like chlorine species, iodine species are known to cluster with bromide ions via halogen (or hydrogen) bonds; as such, here we explore using the Br-CIMS to measure gas-phase iodine species and sulfuric acid simultaneously at concentrations ~~relavant~~relevant to the marine boundary layer. In this study, we demonstrate the detection of various gas-phase inorganic iodine species with the Br-CIMS and explore the effect of relative humidity (RH) on that detection. We then quantify the sensitivities of several gas-phase ~~halogen~~ iodine species via inter-method calibration, offline calibration, and quantum chemical calculations. Finally, we compare the performance of Br-MION-CIMS and Br-FIGAERO-CIMS and show that both of them are well-suited for iodine species measurement in the ~~atmosphere~~marine boundary layer.

2 Methodology

2.1 The CLOUD facility

We conducted measurements and instrument inter-comparison at the CERN CLOUD facility, a 26.1 m³ electropolished stainless-steel chamber that enables new-particle formation experiments simulating the typical range of tropospheric conditions with scrupulous cleanliness and minimal contamination (Duplissy et al., 2016; Kirkby et al., 2011). The CLOUD chamber is mounted in a thermal housing, capable of keeping temperature constant in a range of -65 °C and +100 °C with ±0.1 °C precision (Dias et al., 2017) and relative humidity commonly between < 0.5 % and 80 %. Photochemical processes are driven by different light sources, including four 200 W Hamamatsu Hg-Xe lamps with significant spectral irradiance between 250 and 450 nm, and an array of 48 green light LEDs at 528 nm with adjustable optical power up to 153 W. Ion-induced nucleation under different ionization levels is simulated with a combination of electric fields (electrodes at ±30 kV at top and bottom of the chamber) which can be turned on to rapidly scavenge smaller ions, and a high-flux beam of 3.6 GeV pions (π^+) which enhances ion production when turned on. Mixing is accelerated with magnetically coupled fans mounted at the top and bottom of the chamber. The characteristic gas mixing time in the chamber during experiments is a few minutes. The loss rate of condensable vapors onto the chamber wall is comparable to the condensation sink in pristine boundary layer environments (e.g. 2.2×10^{-3} s⁻¹ for H_2SO_4 at 5 °C). To avoid a memory effect between different experiments, the chamber is periodically cleaned by rinsing the walls with ultra-pure water and heating to 100 °C for at least 24 hours, ensuring extremely low contaminant levels of sulfuric acid ($< 5 \times 10^4$ cm⁻³) and total organics (< 150 pptv) (Kirkby et al., 2016; Schnitzhofer et al., 2014). The CLOUD gas system is also built to the highest technical standards of cleanliness and performance.

The dry air supply for the chamber is provided by cryogenic nitrogen (Messer, 99.999 %) and cryogenic oxygen (Messer, 99.999 %) mixed at the atmospheric ratio of 79:21. Ultrapure water vapor, ozone and other trace gases can be precisely added to attain desired mixing ratios at different levels. The total injection rate of the humidified air is

119 fixed at 330 standard liters per minute (slpm) to compensate for the sampling consumption of various instruments.
120 Molecular iodine (I_2) is injected into the chamber by passing a flow of cryogenic nitrogen through a crystalline iodine
121 (I_2, Sigma-Aldrich, 99.999 % purity) reservoir, which is temperature-controlled at 10 ℃, to achieve levels of 0.4 to
122 168 pptv in the chamber. The sulfinert-coated injection lines are temperature stabilized to minimize line conditioning
123 effects. High intensity green light emitting diodes (LEDs) are used to photolyze molecular iodine into iodine atoms
124 and initiate the subsequent oxidation reactions in the presence of ozone and water vapor. The 48 green LEDs (light
125 sabre 4, LS4) are mounted in pairs (one upward facing, one downward facing) on a copper cooling bar within a long
126 quartz jacket that protrudes into the chamber in the mid plane. The maximum total optical power output is 153 W,
127 centered on 528 nm. Actinic fluxes are regulated by controlling the number of LEDs used and the set point of
128 individual LEDs. Light fluxes are monitored by two photodiodes and a spectrometer. The dry air supply for the
129 chamber is provided by cryogenic oxygen (Messer, 99.999 %) and cryogenic nitrogen (Messer, 99.999 %) mixed at
130 the atmospheric ratio of 79:21. Ultrapure water vapor, ozone and other trace gases can be precisely added to attain
131 mixing ratios at different levels.

2.2 Br-MION-CIMS

134 We measured gas-phase iodine species with a bromide chemical ionization atmospheric pressure interface time-of-
135 flight mass spectrometer (Junninen et al., 2010) coupled with a Multi-scheme chemical IONization inlet (Br-MION-
136 CIMS) (Rissanen et al., 2019). The Br-MION inlet consists of an electrically grounded 24 mm inner diameter stainless
137 steel flow tube, attached to an ion source. For the CLOUD measurements, the length of the sampling inlet was ~1.5
138 m and was designed to be in a laminar flow with a fixed total flow rate of 20 32 standard liters per minute (slpm). An
139 ion filter, operated with positive and negative voltage, was placed at the front of the inlet to filter out any ions in the
140 sample air prior to ion-molecule reaction chamber in the inlet. The reagent ions, bromide (Br^-) and the bromide-water
141 cluster ($H_2O·Br^-$), were produced by feeding 25 standard milliliters per minute (mlpm) of nitrogen (N_2) flow through
142 a saturator containing dibromomethane (CH_2Br_2; > 99.0 %, Tokyo Chemical Industry) into the ion source, where the
143 reagent was ionized by soft X-ray radiation. The resulting ions were then accelerated by a 2850 0 V ion accelerator
144 array and focused by a 2950 V ion deflector into the laminar sampling flow of the inlet via a 5 mm orifice. A small
145 counter flow (~40 mlpm) was applied through the orifice to prevent any mixing of the electrically neutral reagent
146 vapor with the sampling flow. The details of the inlet design, setup, and operation are described in previously (He,
147 2017; Rissanen et al., 2019).

2.3 Br-FIGAERO-CIMS

150 We also measured both the gas- and particle-phase compositions via thermal desorption using a bromide chemical
151 ionization time-of-flight mass spectrometer equipped with a Filter Inlet for Gases and AEROsols (Br-FIGAERO-
152 CIMS) (Lopez-Hilfiker et al., 2014). FIGAERO is a manifold inlet for a CIMS with two operating modes. In the
153 sampling mode, gases are directly sampled into a 150 mbar ion-molecule reactor, using coaxial core sampling to
154 minimize their wall losses in the sampling line. The total flow is maintained at 18.0 slpm and the core flow at 4.5 slpm;
155 the CIMS samples at the center of the core flow with a flow rate at ~1.6 slpm. Concurrently, particles are collected on

156   a PTFE filter via a separate dedicated port with a flow rate of 6 slpm. In the desorption mode, the filter is automatically

157   moved into a pure N_2 gas stream flowing into the ion molecule reactor, while the N_2 is progressively heated upstream

158   of the filter to evaporate the particles via temperature programmed desorption. Analytes are then chemically ionized

159   by Br^- and extracted into a mass spectrometer.

160

161   We optimize the adduct-ion signals in both the Br-MION-CIMS and Br-FIGAERO-CIMS by tuning the electric field

162   strengths in the first two low-pressure stages of the mass spectrometer as weak as possible to minimize collision

163   induced cluster fragmentation while maintaining sufficient ion transmission. Optimization is achieved by maximizing

164   the ratio of I_2Br^-/Br^- at a constant I_2 concentration. We list relevant instrument specifications and operational

165   conditions in Table S1. It should be noted that these values are specific to our instruments, thus can vary according to

166   instrument parameters and may not be applicable to other instruments.

167

168   **2.4 CE-DOAS**

169   For the quantitative measurement of gas-phase molecular iodine (I_2), we deployed a Cavity Enhanced Differential

170   Optical Absorption Spectroscopy instrument (CE-DOAS) (Meinen et al., 2010). CE-DOAS determines concentrations

171   of trace gases from the strength of differential spectral features in a reference spectrum. The overall accuracy for the

172   I_2 time series is estimated to be 20 %, never better than the detection limit (3-sigma precision), resulting from the

173   uncertainty in cross sections and the stability of the baseline. ~~The accuracy of the method is ultimately determined by~~

174   ~~the uncertainty of the respective absorption cross sections.~~ It is thus an absolute method and does not depend on an

175   instrument specific detection efficiency. To maximize the measurement sensitivity towards I_2, we used a setup

176   optimized for the green wavelength range (508-554 nm), where I_2 exhibits strong differential absorption features. The

177   measurement light is provided by a green light emitting diode (LED Engin). Spectral dispersion is established with a

178   Czerny-Turner grating spectrometer (Princeton Instruments Acton 150), resulting in an optical resolution of 0.73 nm

179   full width at half maximum at 546 nm. Intensities are monitored with a CCD detector (Princeton Instruments

180   PIXIS400B) cooled to -70 °C. Highly reflective mirrors (Advanced Thin Films) enhance the 1 m mirror separation to

181   an effective optical path length of 15-23 km. The effective spectral mirror reflectivity was established by comparing

182   light intensity spectra in the presence of N_2 and He (Washenfelder et al., 2008). The abundance of trace gases is then

183   determined by comparing spectra of chamber air relative to reference spectra recorded with ultrapure N_2 without I_2.

184   Chamber air is drawn into the cavity with a constant flow rate of 1 slpm. Variations of the sampling flow did not result

185   in changes in measured I_2 concentrations, indicating that photolysis from the measurement light within the instrument

186   was negligible. The following absorbers were included in the fit: I_2 (Spietz et al., 2006), NO_2 (Vandaele et al., 1998),

187   H_2O (Rothman et al., 2010), O_2-O_2 collision-induced absorption (Thalman and Volkamer, 2013), and a polynomial of

188   sixth order. The setup allowed a 1-minute detection limit of 25 pptv, or 8 pptv for integration times of 10 minutes,

189   respectively. Periodic automated recordings of N_2 reference spectra were recorded to ensure baseline stability. The

190   optical path length at the time of measurement was continuously confirmed for consistency by the measurement of

191   the O_2-O_2 collision-induced absorption and H_2O column in the same analysis window. The overall systematic accuracy

192 for the I_2 time series is estimated to be 20 %, never better than the detection limit, resulting from the uncertainty in

193 cross sections and the stability of the baseline.

194

195 **2.5 Offline calibration setup**

196 **2.5.1 I_2 permeation device**

197 We used an iodine permeation tube (VICI Metronic) as a source for offline laboratory calibration. The permeation

198 tube was encased within an electronically controlled heating mantle (80 ~ 140 (± 2) °C) to allow for adjustable yet

199 steady iodine permeation rates. The heating device (for holding the permeation tube) was made from a stainless steel

200 tube (½-inch outer diameter, OD) with a length of 25 cm, encased within an electronically controlled heating mantle.

201 The configuration of the permeation device has been described in Tham et al. (Tham et al., 2021). The iodine

202 permeation device was run continuously for at least 72 hours before any calibration experiments to ensure that a

203 complete equilibrium was reached in the system. We then confirmed the robustness of the permeation device by the

204 constant I_2 signal measured with Br-MION-CIMS for over 24 hours.

205

206 To determine the permeation rate of I_2, we trapped iodine in n-hexane at cryogenic temperatures in an all-glass

207 apparatus, following the method described in Chance et al. (Chance et al., 2010). We initially filled the absorption

208 glass vessel with 20 ml n-hexane (99.95 %, Merck), and then weighed it to determine the combined mass. We then

209 immersed the absorption vessel into a wide-necked Dewar vessel, filled with an acetone/dry ice mixture (at −80 ±

210 3 °C). After temperature equilibration, the I_2 molecules, carried by 50 mlpm N_2 flow from the permeation device, were

211 bubbled through the absorption vessel. After a continuous collection for 5 hours, we removed the absorption apparatus

212 from the cooling mixture, and allowed it to warm to room temperature prior to disassembling the setup to prevent any

213 losses of iodine on the tip of the inlet capillary. The absorption vessel was then re-weighed; the mass compared with

214 that prior to absorption was less than 2 %, indicating a negligible loss during the trapping process. The I_2 / n-hexane

215 sample solutions were stored at 4 °C for 14 hours before being subjected to analysis.

216

217 We determined the I_2 concentration of the samples using a UV/Vis spectrophotometer (Shimadzu Model UV2450) at

218 a wavelength of 522 nm. We established a calibration curve via a set of I_2 solutions ranging from 270 to 5300 nmol,

219 diluted with n-hexane from a freshly prepared stock solution (0.5 g L^{-1}). Repetition of the same analysis after 2 and 7

220 days yielded identical results, confirming that the sample solutions were stable at 4 °C. As an alternative analytical

221 approach, we also quantified the I_2 concentration in the sample solutions using an inductively coupled plasma mass

222 spectrometer (ICP-MS, Agilent 7800). Before introducing to the ICP-MS, the sample solutions were treated with

223 $NaHSO_3$ water solution (0.100 M), accomplishing efficient hexane-to-water extraction and simultaneous reduction of

224 iodine to iodide (Schwehr et al., 2005) (Agilent Clinical Sample Preparation Guide (v3), *ref.* ISO 17294-2). The ICP-

225 MS results were in good agreement (within 20 % discrepancies) with those from the UV/Vis spectrophotometry.

226

227 We conducted the I_2 trapping and quantification experiments in triplicate with satisfactory reproducibility (standard

228 deviation < 10 %). The calculated iodine permeation rate at 50 mlpm N_2 flow and 140 °C oven temperature is 278 ±

229 12 ng min^{-1} (mean ± standard deviation). This result was used as the benchmark to estimate temperature-corrected

230 permeation rates according to the formula provided by the permeation tube vendor (VICI Metronic). We checked the

231 validity of the temperature-corrected values by conducting a second iodine absorption experiment in which the iodine

232 permeation tube was kept at 130 °C with an N_2 flow rate of 50 mlpm, and the determined permeation rate agreed

233 within 10 % of the calculated value.

2.5.2 Cl_2 permeation device

236 We used a commercial chlorine permeation tube (VICI Metronic) as a source for offline calibration. We passed a 20

237 mlpm high-purity nitrogen (99.999 %) flow at room temperature through a 25 cm long stainless-steel tube (½" O.D.)

238 containing the permeation tube. We quantified the permeation rate of Cl_2 following a procedure described in a previous

239 study (Finley and Saltzman, 2008). The output of 20 mlpm flow was bubbled into a buffered aqueous potassium iodide

240 solution (2.0 % KI (*m/v*), prepared in 1.00 mM aqueous phosphate buffer, pH = 7.0) filled in an all-glass two-stage

241 serial absorption apparatus (stage 1 = 100 ml; stage 2 = 50 ml) for 3 hours and kept at room temperature. The Cl_2

242 oxidized the iodide (I^-) into iodine (I_2) once contacting with the KI absorption solution, and the I_2 further reacted with

243 the excess KI present in the absorption solution to form I_3^-, which can be quantified by UV/Vis-spectrophotometry.

244 We analyzed the resulting sample solutions with an UV/Vis spectrophotometer (Shimadzu Model UV-1800) using 1-

245 cm quartz cells at 352 nm, corresponding to the I_3^-. We detected no I_3^- in the second stage absorption solution,

246 indicating that all the chlorine was quantitatively trapped and rapidly converted to I_3^- within the first absorption unit.

247 The samples were quantified relative to I_3^- standards in the range of 5 to 68×10^{-6} M, prepared by dilution of a stock

248 obtained by dissolving 174 mg iodine in 200 ml of a solution containing 2 % KI in 1.00 mM aqueous phosphate buffer,

249 pH 7.0. From this calibration curve, we calculated a molar absorptivity of 26,800 L mol^{-1} cm^{-1}, which is consistent

250 with the values reported in the literature (Finley and Saltzman, 2008; Kazantseva et al., 2002). Samples and standard

251 solutions were re-analyzed after being stored in the dark at room temperature for 24 hours, and the results were within

252 3 % of those obtained with the fresh solutions. We repeated the absorption experiment, and the calculated chlorine

253 permeation rate at room temperature was 764 ± 74 ng Cl_2 min^{-1} (mean ± standard deviation).

2.5.3 HOI calibrator

256 We produced a continuous HOI source via the reaction of I_2 and hydroxyl radicals (OH) in a setup similar to the

257 sulfuric acid (H_2SO_4) calibrator (Kürten et al., 2012). The OH was generated by photolyzing H_2O with a mercury (Hg)

258 lamp at 184.9 nm, whose calibrated intensity was used to estimate the OH concentration. We tested the system by

259 removing the I_2 or OH source from the calibrator, upon which HOI production was undetectable, confirming that any

260 single reactant did not produce HOI. A numerical model was constructed to predict the mean HOI concentration

261 entering the Br-MION-CIMS, which is analogous to the model used for H_2SO_4 calibration (Kürten et al., 2012). We

262 only included the formation pathway of I_2 + OH to HOI in the model for simplicity; the other pathway of IO + HO_2

263 was considered minor as its reaction rate is about an order of magnitude slower than that of I_2 + OH. Furthermore, IO

264 is likely at negligible concentration in the calibration device due to the absence of O_3 for IO formation.

2.65 Quantum chemical calculations

We used quantum chemical calculations to estimate the cluster formation enthalpy of halogen containing species and bromide ions. The initial conformational conformer sampling was performed using the Spartan '14 program. The cluster geometry was then optimized using density function theory methods at the ωB97X-D/aug-cc-pVTZ-PP level of theory (Chai and Head-Gordon, 2008; Kendall et al., 1992). Iodine pseudopotential definitions were taken from the EMSL basis set library (Feller, 1996). Calculations were carried out using the Gaussian 09 program (Frisch et al., 2010). An additional coupled-cluster single-point energy correction was carried out on the lowest energy geometry to calculate the final cluster formation enthalpy. The coupled-cluster calculation was performed at the DLPNO-CCSD(T)/def2-QZVPP level using the ORCA program ver. 4.0.0.2 (Neese, 2012; Riplinger and Neese, 2013). In Table 1 we present calculated cluster formation enthalpies based on the optimized geometries.

3 Results and Discussion

3.1 Detection of gas-phase inorganic species by Br-MION-CIMS

We show in Fig. 1 the selected inorganic species observed with the Br-MION-CIMS during an iodine new particle formation oxidation experiment in the CLOUD chamber. The peak identities are indicated in the labels. Observed species include I_2 and its various oxidation products. There are also a few other halogen-containing inorganic species such as Cl_2, ICl and IBr, likely coming from the impurities in the iodine source. Non-halogen inorganic species such as H_2SO_4 can also react with bromide ions and are detected. Due to the large negative mass defect of the bromine and iodine atoms, and the high resolution (~10000 Th Th^{-1}) of the mass spectrometer, the peaks can be unambiguously distinguished and identified in the mass spectrum. As shown in the lower panel of Fig. 1, most of the iodine-containing species appear as a single peak in the unit mass range, except for $HIO_2 \cdot {}^{79}Br^-$ (m/z = 238.82), which overlaps with the reagent ion cluster $({}^{79}Br_2{}^{81}Br)^-$ (m/z = 238.75).

The iodine <u>oxidation</u> <s>new particle formation</s> experiments were conducted under experimental conditions typically found in the high-latitude marine boundary layer, with a temperature of -10 °C and a relative humidity of 69 %. As illustrated in Fig. 2, a typical experiment started with illumination of the chamber at constant I_2 (~60 pptv) using the green light to photolytically produce I atoms. The subsequent reactions of I and ~ 40 ppbv O_3 led to the formation of various oxidized iodine species within a few minutes. The most prominent species we observed from these experiments were IO, HOI and HIO_3, with lower but significant levels of OIO, HIO_2, and I_2O_4. Among these iodine

oxides, IO rose the most rapidly; this is consistent with the first-generation production of IO from the I + O₃ reaction. After a few steps of radical reactions, OIO, HIO₂ and HIO₃ reached steady state almost simultaneously. The only observed iodine oxide dimer was I₂O₄ in this event, while I₂O₂, I₂O₃ and I₂O₅ were below the detection limit of both mass spectrometers. A noticeable dip in the HIO₃ traces a few minutes after the onset of the reactions is likely due to the participation of HIO₃ in new-particle formation, resulting in an extra loss term and a lower steady-state concentration. When we turned off the green light, the production of I radicals stopped and iodine species decayed away.
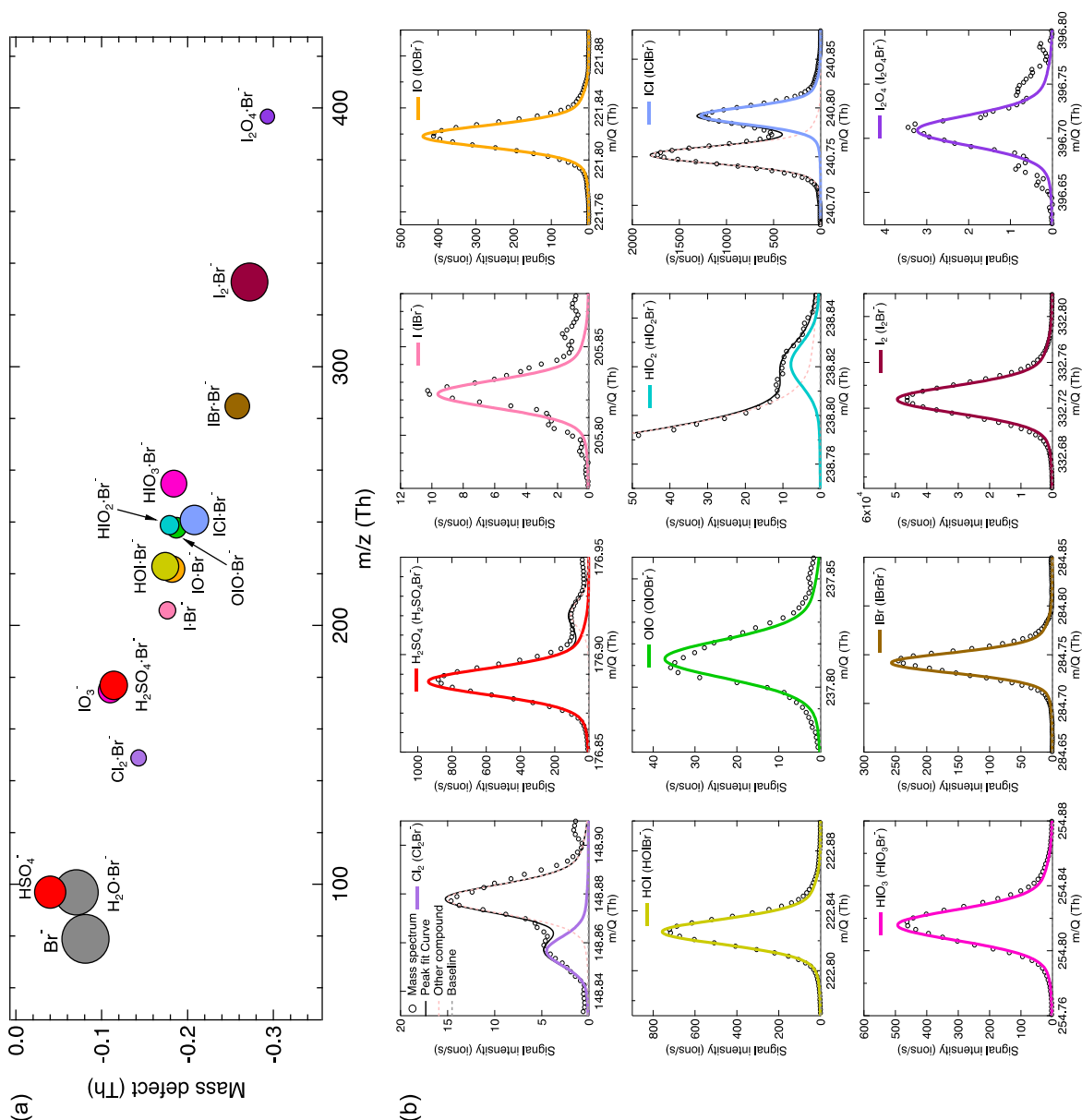
Figure 1. Gas-phase inorganic species measured with the Br-MION-CIMS. (a) Mass defect (difference of exact mass to integer mass) versus m/z of gas-phase halogen species and sulfuric acid during an iodine oxidation experiment at 69 % relative humidity and -10 °C (conducted on 05 October 2018). Ions shown here are either clustered with or formed via proton transfer to a bromide ion. The area of the markers is proportional to the logarithm of the signal (counts per second). (b) The high-resolution single peak fits for species in the mass defect plot in the upper panel. Species in both panels are color-coded in the same style.

315
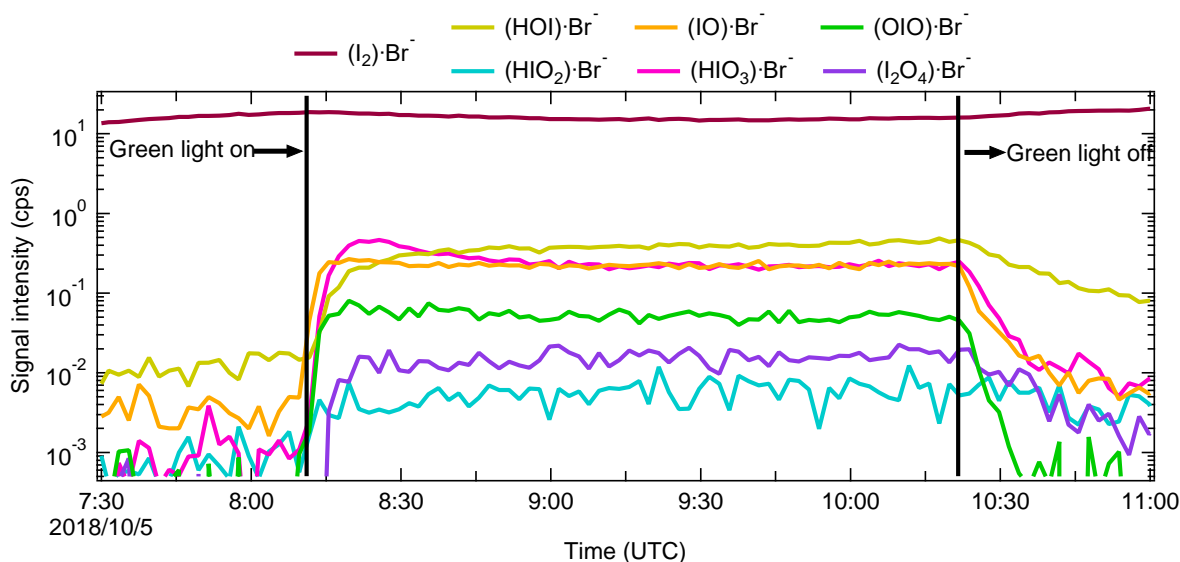
Figure 2. Evolution of selected iodine species during a typical run. The experiment was performed at 60 pptv I_2, 40 ppbv O_3, 69 % relative humidity and -10 °C. The oxidized iodine species start to appear soon after switching on the green light at 08:11, 05 October 2018. The I atom production was halted at 10:21, 05 October 2018 by switching off the green light, and the concentration of oxidized iodine species decayed away afterwards. All species are color-coded in the same way as in Fig. 1.

3.2 Relative humidity dependence

Water molecules can cluster with I^- to form $H_2O \cdot I^-$ in the iodide CIMS. This enhances the instrument sensitivities for small molecules (i.e. chlorine and bromineinorganics) and reduces them for large molecules (i.e. oxygenated organics) (Lee et al., 2014). To investigate the role of water concentration in the sensitivity of the Br-MION-CIMS, we varied the relative humidity (RH) from 40 % to 80 % at a constant temperature of -10 °C. We show in Fig. 3 the correlation of I_2 time series from the Br-MION-CIMS and the CE-DOAS throughout the experiment.

Chemical ionization relies on an ion-molecule reaction to transfer charge from a reagent ion to an analyte, forming either a product ion or a charged cluster between the analyte and the reagent ion with a rate coefficient k_{IM}. This occurs in an ion-molecule reactor, with a fixed flow rate and thus reaction time, dt, and ideally under pseudo first-order conditions where a small fraction of the analyte is ionized and the reagent ion concentration ([Ion]) remains constant. Under these (linear) conditions the fraction of analyte that is ionized is $k_{IM} \times$ [Ion] $\times d$t. However, the primary ion source strength can vary with time, and so we normalize the analyte signal by reagent ion signal to account for those small variations in analyte signal.

During the RH transition, the ratio of the two reagent ions, Br^- and $H_2O \cdot Br^-$, changed in the Br-MION-CIMS. As shown in Fig. 3 (a) and (b), using either reagent ion alone for I_2 normalization results in discrepancies in recovered I_2 concentrations at different RH. However, if we use the sum of these two reagent ions ($Br^- + H_2O \cdot Br^-$) for normalization, the humidity effect vanishes, as shown in the-Fig. 3 (c). Separately, during the I_2 calibration using a permeation tube (section 3.3.2.1), This suggests that the quantitative detection of I_2 molecules is robust and independent of RH between 20 % and 40 % at 25 °C, as long as a proper normalization method is used for the Br-MION-CIMS. Furthermore, we

343   have also carried out the HOI calibration at 25 °C (section 3.3.2.3) and used the same normalization method as

344   described in section 3.3.4. During the calibration, we varied the water content in the calibrator to vary OH

345   concentrations. A good correlation between the modeled HOI concentrations and the measured HOI signals also

346   indicates that the different H_2O concentrations in the system do not affect the HOI detection (Fig.4(d)). This assertion

347   may also be applicable to other molecules such as iodine monochloride (ICl) and iodine monobromide (IBr), which

348   share similar chemical and physical properties with I_2; , buthowever, further confirmation is needed for other species

349   such as oxygenated organics.

350
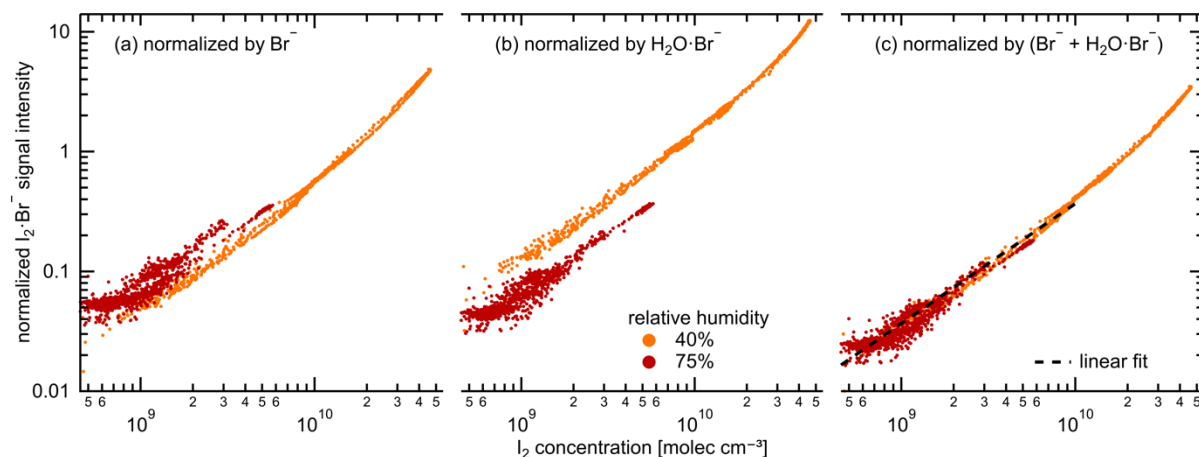
351
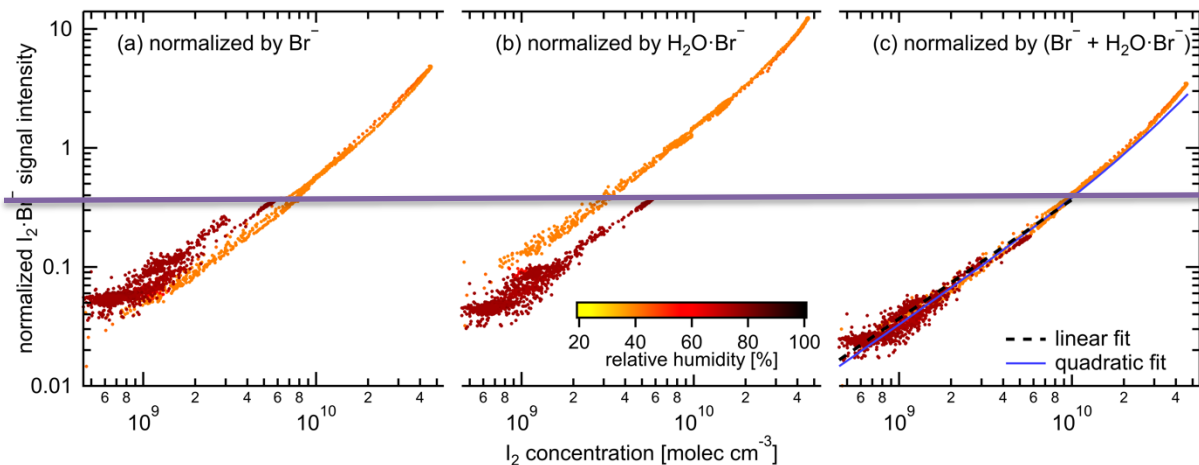
352

353 **Figure 3.** Signal normalization methods for the Br-MION-CIMS. Normalized $I_2 \cdot Br^-$ signal intensity for variable I_2 concentrations,

354 color coded by relative humidity (orange: 35-45 % relative humidity, red: 70-80 % relative humidity). The charger ions in the ion

355 source of Br-MION-CIMS are Br^- and $H_2O \cdot Br^-$ (both ^{79}Br and ^{81}Br). Their abundance depends both on the instrument tuning and

356 the absolute humidity of the sampled flow. The normalization of the $I_2 \cdot Br^-$ signal by only Br^- (a) or $H_2O \cdot Br^-$ (b) does not compensate

357 for the humidity effect. Using the sum of Br^- and $H_2O \cdot Br^-$ (c) for normalization yields a tight correlation to the true I_2 as measured

358 by CE-DOAS, independent of the humidity. The black dashed line and blue solid curve indicates the fitted linear and quadratic

359 calibration curves, respectively.

360

3.3 Quantification of gas-phase inorganic species

362 Inter-method calibrations and offline calibrations were carried out to quantify the sensitivities of the Br-MION-CIMS

363 to selected calibrants. For the inter-method calibrations, we used the CLOUD chamber as a stable source of I_2 and

364 H$_2$SO$_4$, and inter-compared the signals in the Br-MION-CIMS with the CE-DOAS and a pre-calibrated nitrate-CIMS,

365 respectively. For the offline calibrations, we carried out the experiments separately in a laboratory at the University

366 of Helsinki, using permeation tubes to quantify I$_2$ and Cl$_2$, and a calibrator to quantify HOI.

367

368 **3.3.1 Inter-method calibrations at CLOUD**

369 **3.3.1.1 I$_2$ calibration using the CE-DOAS**

370 As shown in Fig. 3, we use the accurate I$_2$ time series measured with the CE-DOAS to calibrate normalized I$_2$ signals

371 in the Br-MION-CIMS. The I$_2$ concentrations used for the calibration span approximately 2 orders of magnitude,

372 reaching up to 4.6×10^{10} molec cm^{-3}. A linear fit, limited to I$_2$ concentrations smaller than 10^{10} molec cm^{-3}, establishes

373 the calibration factor as follows:

374 $$[I_2] = 2.7 \times 10^{10} \text{ molec cm}^{-3} \times I_2 \cdot {}^{79}Br^-/({}^{79}Br^- + H_2O \cdot {}^{79}Br^-)$$

375 For this range of concentrations, which are typically encountered in the atmosphere, the calibrated Br-MION-CIMS

376 time series agrees within error with the CE-DOAS measurement (1-sigma accuracy 20 %, detection limit 25 pptv for

377 1 min data). Deviations between both time series are generally smaller than 10 % (25 and 75 percentile 0.88 and 1.03,

378 respectively). These small differences may be explained by incomplete homogeneity of iodine concentrations in the

379 chamber and the different sampling positions of CE-DOAS and Br-MION-CIMS. ~~As shown in Fig. 3, we use the~~

380 ~~accurate I$_2$ time series measured with the CE-DOAS to calibrate normalized I$_2$ signals in the Br-MION-CIMS. The I$_2$~~

381 ~~concentrations used for the calibration span approximately 2 orders of magnitude, reaching up to 4.6×10^{10} molec cm$^-$~~

382 ~~^{3}. A linear fit, limited to I$_2$ concentrations smaller than 10^{10} molec cm^{-3}, establishes the calibration factor [I$_2$] = 2.7×10^{10}~~

383 ~~molec cm^{-3} × I$_2$·^{79}Br$^-$/(^{79}Br$^-$ + H$_2$O·^{79}Br$^-$). We also use a quadratic fit to establish the calibration for the entire range of~~

384 ~~concentrations encountered during whole campaign (solid line in Fig. 3 (c)); two curves agree well. The CE-DOAS I$_2$~~

385 ~~detection limit is 6.3×10^8 molec cm^{-3} (25 pptv) for a 1 min integration time, and the total systematic uncertainty is~~

386 ~~estimated to be 20%. Deviations between both time series are generally smaller than 10% (25 and 75 percentile 0.88~~

387 ~~and 1.03, respectively). These small differences are consistent with incomplete homogeneity of iodine concentrations~~

388 ~~in the chamber and the different sampling positions of CE-DOAS and Br-MION-CIMS.~~

389

390 **3.3.1.2 H$_2$SO$_4$ calibration using a nitrate-CIMS**

391 We derive the H$_2$SO$_4$ calibration coefficient for the Br-MION-CIMS using the absolute H$_2$SO$_4$ concentrations

392 measured with a pre-calibrated nitrate-CIMS. The calibration protocol of H$_2$SO$_4$ in the nitrate-CIMS has been

393 described in detail previously (Kürten et al., 2012). The H$_2$SO$_4$ time series used for the inter-method calibration covers

394 a wide concentration range from less than 5.0×10^4 (detection limit of the nitrate-CIMS) to 6.0×10^7 molec cm^{-3}. For

395 Br-MION-CIMS, although both HSO$_4^-$ and H$_2$SO$_4$·Br$^-$ appear as distinct peaks for sulfuric acid, we only use the

396 normalized H$_2$SO$_4$·^{79}Br$^-$ for the inter-calibration, as HSO$_4^-$ (m/z = 96.96) has substantial interference from the reagent

397 ion H$_2$O·^{79}Br$^-$ (m/z = 96.93). We show in Fig. 4 (a) the linear fit:

398 $$[H_2SO_4] = 4.1 \times 10^{10} \text{ molec cm}^{-3} \times H_2SO_4 \cdot {}^{79}Br^-/({}^{79}Br^- + H_2O \cdot {}^{79}Br^-) - 9.3 \times 10^5)$$

The H_2SO_4 calibration coefficient is thus 4.1×10^{10} molec cm^{-3} per normalized signal (cps cps^{-1}), and the correlation coefficient between the two H_2SO_4 traces is 0.95. The systematic 3-sigma accuracy is +50/-33 % for H_2SO_4 calibration using a nitrate-CIMS; detailed accuracy estimation has been discussed previously (Stolzenburg et al., 2020).

3.3.2 Offline laboratory calibrations for I_2, Cl_2, and HOI

I_2 calibration using a permeation tube

We used an iodine permeation tube (VICI Metronic) as a source for offline calibration. The permeation tube was encased within an electronically controlled heating mantle (80 ~ 140 ($\pm$ 2) °C) to allow for adjustable yet steady iodine permeation rates. The iodine permeation device was run continuously for at least 72 hours before any calibration experiments to ensure that a complete equilibrium was reached in the system. We then confirmed the robustness of the permeation device by the constant I_2 signal measured with Br-MION-CIMS for over 24 hours.

To determine the permeation rate of I_2, we trapped iodine in n hexane at cryogenic temperatures in an all glass apparatus, following the method described in Chance et al. (Chance et al., 2010). We initially filled the absorption glass vessel with 20 ml n hexane (99.95%, Merck), and then weighed it to determine the combined mass. We then immersed the absorption vessel into a wide-necked Dewar vessel, filled with an acetone/dry ice mixture (at −80 $\pm$ 3 °C). After temperature equilibration, the I_2 molecules, carried by 50 mlpm N_2 flow from the permeation device, were bubbled through the absorption vessel. After a continuous collection for 5 hours, we removed the absorption apparatus from the cooling mixture, and allowed it to warm to room temperature prior to disassembling the setup to prevent any losses of iodine on the tip of the inlet capillary. The absorption vessel was then re-weighed; the mass compared with that prior to absorption was less than 2%, indicating a negligible loss during the trapping process. The I_2 / n hexane sample solutions were stored at 4 °C for 14 hours before being subjected to analysis.

We determined the I_2 concentration of the samples using a UV/Vis spectrophotometer (Shimadzu Model UV2450) at a wavelength of 522 nm. We established a calibration curve via a set of I_2 solutions ranging from 270 to 5300 nmol, diluted with n-hexane from a freshly prepared stock solution (0.5 g L^{-1}). Repetition of the same analysis after 2 and 7 days yielded identical results, confirming that the sample solutions were stable at 4 °C. As an alternative analytical approach, we also quantified the I_2 concentration in the sample solutions using an inductively coupled plasma mass spectrometer (ICP MS, Agilent 7800). Before introducing to the ICP MS, the sample solutions were treated with NaHSO$_3$ water solution (0.100 M), accomplishing efficient hexane-to-water extraction and simultaneous reduction of iodine to iodide (Schwehr et al., 2005) (Agilent Clinical Sample Preparation Guide (v3), *ref.* ISO 17294-2). The ICP-MS results were in good agreement with those from the UV/Vis spectrophotometry.

We conducted the I_2 trapping and quantification experiments in triplicate with satisfactory reproducibility (standard deviation < 10%). The calculated iodine permeation rate at 50 mlpm N_2 flow and 140 °C oven temperature is 278 $\pm$ 12 ng min^{-1} (mean $\pm$ standard deviation). This result was used as the benchmark to estimate temperature corrected permeation rates according to the formula provided by the permeation tube vendor (VICI Metronic). We checked the

14

validity of the temperature-corrected values by conducting a second iodine absorption experiment in which the iodine permeation tube was kept at 130 °C with an N_2 flow rate of 50 mlpm, and the determined permeation rate agreed within 10% of the calculated value. WeFor the I_2 calibration, we then diluted the I_2 flow to seven different values and measured the flow with the Br-MION-CIMS. We repeated the calibration five times; we show the data along with a linear fit between the I_2 concentration and normalized I_2 signal in Fig. 4 (ab). The slope of the line gives a calibration coefficient of 6.3×10^{10} molec cm^{-3} per normalized signal (cps cps^{-1}), with R^2 of 0.98 and an overall 1-sigma accuracy uncertainty of $\pm$ 45 %.

### 3.3.3 Cl$_2$ calibration using a permeation tube

We used a commercial chlorine permeation tube (VICI Metronic) as a source for offline calibration. We passed a 20 mlpm high-purity nitrogen (99.999%) flow at room temperature through a 25-cm long stainless-steel tube (½" O.D.) containing the permeation tube. We quantified the permeation rate of Cl$_2$ following a procedure described in a previous study (Finley and Saltzman, 2008). The output of 20 mlpm flow was bubbled into a buffered aqueous potassium iodide solution (2.0 % KI (m/v), prepared in 1.00 mM aqueous phosphate buffer, pH = 7.0) filled in an all-glass two-stage serial absorption apparatus (stage 1 = 100 ml; stage 2 = 50 ml) for 3 hours and kept at room temperature. The Cl$_2$ oxidized the iodide (I$^-$) into iodine (I$_2$) once contacting with the KI absorption solution, and the I$_2$ further reacted with the excess KI present in the absorption solution to form I$_3^-$, which can be quantified by UV/Vis spectrophotometry. We analyzed the resulting sample solutions with an UV/Vis spectrophotometer (Shimadzu Model UV-1800) using 1-cm quartz cells at 352 nm, corresponding to the I$_3^-$. We detected no I$_2^-$ in the second-stage absorption solution, indicating that all the chlorine was quantitatively trapped and rapidly converted to I$_3^-$ within the first absorption unit. The samples were quantified relative to I$_3^-$ standards in the range of 5 to 68 × 10^{-6} M, prepared by dilution of a stock obtained by dissolving 174 mg iodine in 200 ml of a solution containing 2 % KI in 1.00 mM aqueous phosphate buffer, pH 7.0. From this calibration curve, we calculated a molar absorptivity of 26,800 L mol^{-1} cm^{-1}, which is consistent with the values reported in the literature (Finley and Saltzman, 2008; Kazantseva et al., 2002). Samples and standard solutions were re-analyzed after being stored in the dark at room temperature for 24 hours, and the results were within 3 % of those obtained with the fresh solutions. We repeated the absorption experiment, and the calculated chlorine permeation rate at room temperature was 764 ± 74 ng Cl$_2$ min^{-1} (mean ± standard deviation).

TheFor the Cl$_2$ calibration, the Cl$_2$ permeation source was run continuously for 12 hours prior to calibration experiments to ensure complete system equilibrium. A two-stage dilution system similar to the setup of (Gallagher et al., 1997) was set up for diluting the output of the Cl$_2$ permeation device. The 20 mlpm of N_2 stream emerging from the Cl$_2$ permeation device (operated at room temperature) was diluted in a stream of 6 slpm of dry N_2. Then, a small fraction of this mixture (50 to 300 mlpm) was further mixed with the total flow of 25 slpm of N_2 (20 slpm dry N_2 + 5 slpm humidified N_2) before being sampled by the Br-MION-CIMS. The calibration coefficient for Cl$_2$ was determined to be 3.5×10^{11} molec cm^{-3} per normalized signal (cps cps^{-1}) from three separate calibration experiments (Fig 4 (bc)), with an 1-sigman accuracy of 30 %.

473 ~~**3.3.4 HOI calibration using a calibrator**~~

474 ~~We produced a continuous HOI source via the reaction of I_2 and hydroxyl radical (OH) in a setup similar to the sulfuric~~

475 ~~acid (H_2SO_4) calibrator (Kürten et al., 2012). The OH was generated by photolyzing H_2O with a mercury (Hg) lamp~~

476 ~~at 184.9 nm, whose calibrated intensity was used to estimate the OH concentration. We tested the system by removing~~

477 ~~the I_2 or OH source from the calibrator, upon which HOI production was undetectable, confirming that any single~~

478 ~~reactant did not produce HOI. A numerical model was constructed to predict the mean HOI concentration entering the~~

479 ~~Br MION CIMS, which is analogous to the model used for H_2SO_4 calibration (Kürten et al., 2012). We only included~~

480 ~~the formation pathway of I_2 + OH to HOI in the model for simplicity; the other pathway of IO + HO_2 was considered~~

481 ~~minor as IO forms at a relatively slow rate via the reaction of I radical and O_3.~~ <u>A</u> ~~W~~<u>s for the HOI calibration, w</u>e

482 produced a range of HOI concentrations by varying I_2 and OH concentrations in the calibrator. We show in Fig. 4 (~~e~~<u>d</u>)

483 the linear correlation between the modeled HOI concentrations and measured HOI signals. The slope of the fit ~~line~~

484 corresponds to a calibration coefficient of 3.3×10^{11} molec cm^{-3} per normalized signal (cps cps^{-1}), with an overall <u>1-</u>

485 <u>sigma accuracy</u> ~~uncertainty~~ of ~~±~~ 55 %. The good correlation ($R^2 = 0.97$) including various H_2O levels also indicates

486 that H_2O concentrations did not affect the HOI detection.

487

16

488

17
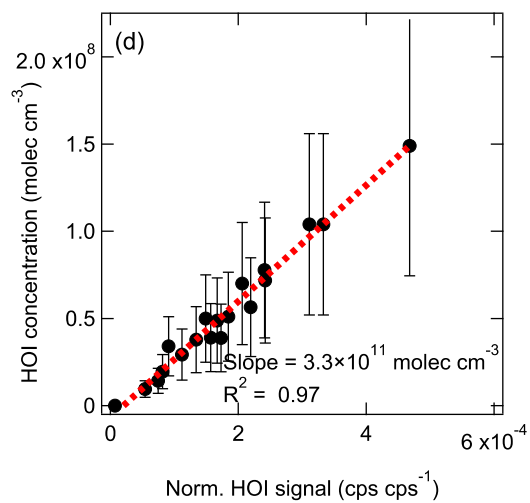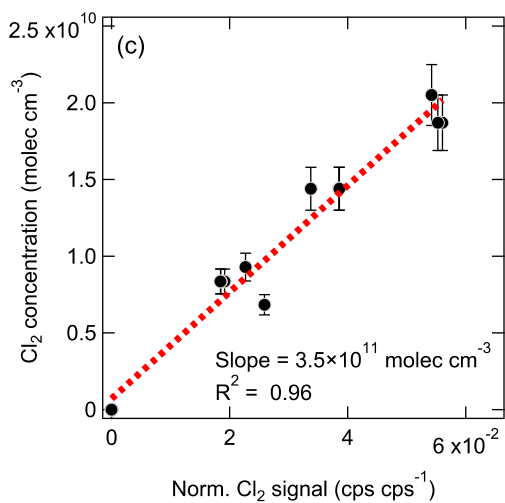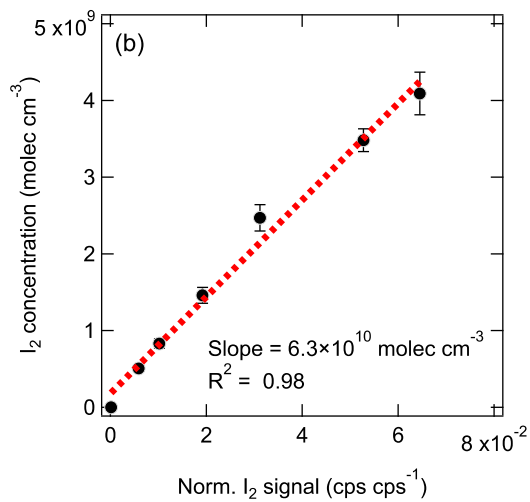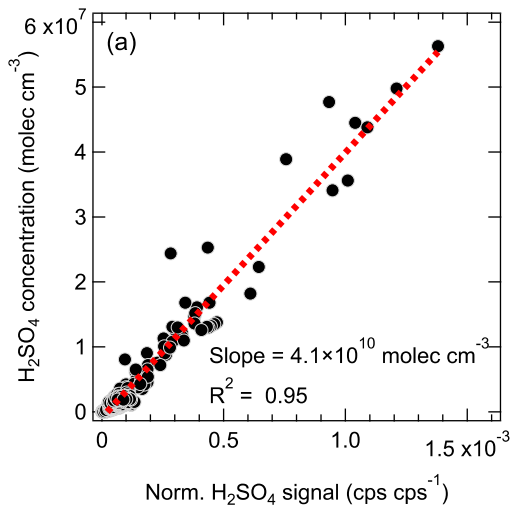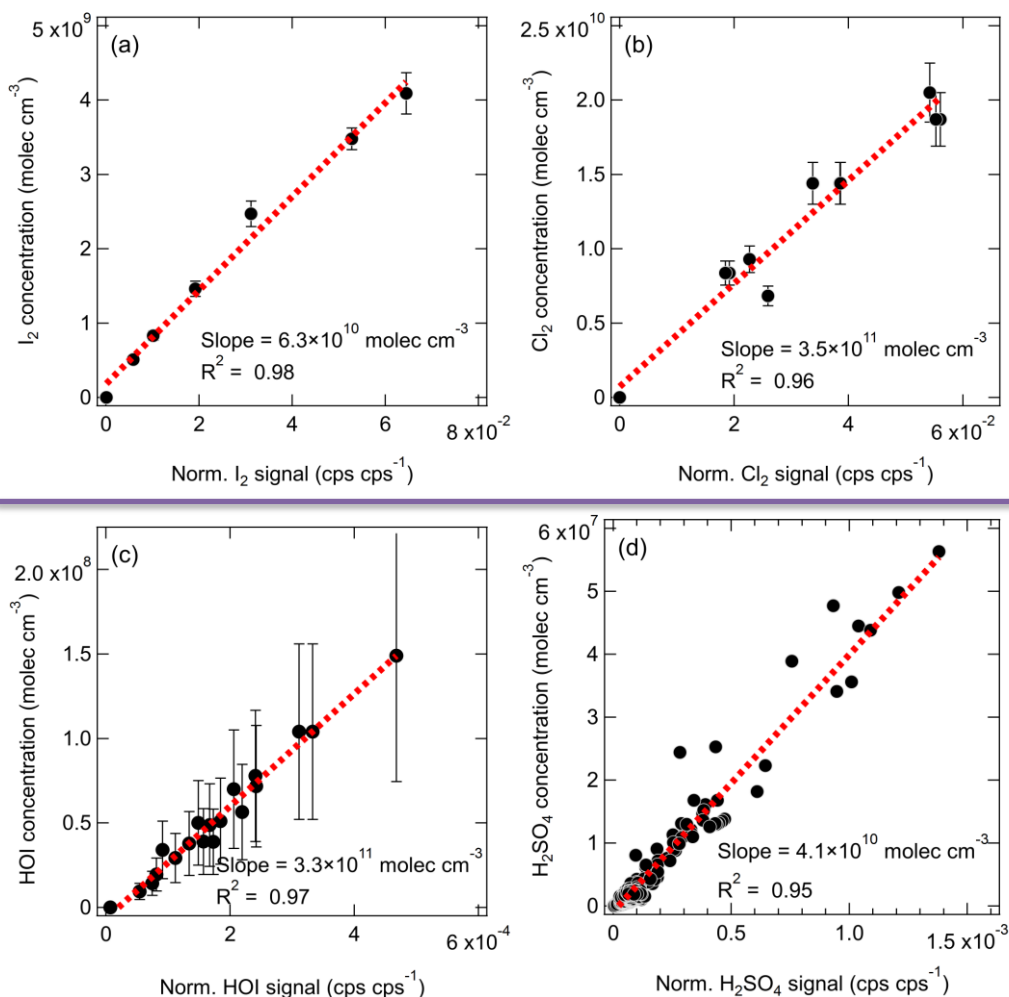
Figure 4. The normalized signals (cps cps^{-1}) ~~absolute concentrations (molec cm^{-3})~~ *vs.* the absolute concentrations (molec cm^{-3}) ~~normalized signals (cps cps^{-1})~~ measured with the Br-MION-CIMS for (a) H$_2$SO$_4$~~I$_2$~~, (b) ~~Cl$_2$~~I$_2$, (c) Cl$_2$~~HOI~~, and (d) HOI ~~H$_2$SO$_4$~~. The red dashed lines are the linear fit~~ting~~s. The overall ~~factor 2 systematic~~ 3-sigma accuracy of +50/-33 % ~~scale uncertainty~~ on [H$_2$SO$_4$] is not shown here.

3.3.3~~6~~ Connecting sensitivity to binding enthalpy

Beyond the species for which we carried out calibrations, there are many more, especially iodine species, that cannot be directly calibrated due to a lack of authentic standards or generation methods. However, the sensitivity of an iodide-CIMS towards analytes can be predicted by the cluster binding enthalpy, calculated by relatively simple quantum chemical methods (Iyer et al., 2016). This holds for the ~~bromide~~Br-CIMS as well. In the instrument, ion clusters, formed from reactions between analytes and reagent ions, are guided and focused by ion optics during transmission to the detector. The electric forces applied to the clusters enhance their collision energies with carrier gas molecules. If sufficient energy is transferred during the collision, cluster fragmentation may occur, affecting the instrument sensitivity for the analytes (Passananti et al., 2019). However, clusters with higher binding enthalpy will be more easily preserved and detected. Analytes that bind to the reagent ions with enthalpies higher than a critical level are likely detected at maximum sensitivity (kinetic-limited detection) by the instrument. For example, the calculated

18

506   critical enthalpy is 25 kcal mol^{-1} for the iodide-CIMS used in Iyer et al. (Iyer et al., 2016) and Lopez-Hilfiker et al.

507   (Lopez-Hilfiker et al., 2016), calculated at the DLPNO-CCSD(T)/def2-QZVPP//PBE/aug-cc-pVTZ-PP level of theory.

508

509   For the bromide chemical ionization, there are two types of fragmentation pathways:

510   1)   Reversion to the original form of Br$^-$ and analyte

511 $$\text{X-H} \cdot \text{Br}^- \rightarrow \text{X-H} + \text{Br}^- \qquad\qquad (1)$$

512   2)   Proton transfer from the analyte to Br$^-$

513 $$\text{X-H} \cdot \text{Br}^- \rightarrow \text{X}^- + \text{HBr} \qquad\qquad (2)$$

514   where the X-H is the hydrogen bond donor. An analyte ~~may be expected to~~should be detected at the maximum

515   sensitivity when the dissociation enthalpy for the first pathway is either a) much higher than the critical enthalpy

516   (dissociation of X-H·Br$^-$ ~~back~~ to X-H and Br$^-$ ~~the reactants~~ does not occur), or b) lower than the critical enthalpy, but

517   much higher than that of the second pathway (dissociation of X-H·Br$^-$ to X-H and Br$^-$ may occur, but dissociation to

518   X$^-$ and HBr ~~back to the reactants would occur, but it is not competitive with the other dissociation channel~~is the

519   dominant pathway). Whether the enthalpy for the second pathway is higher than the critical enthalpy does not directly

520   affect the sensitivity, as both X-H·Br$^-$ and X$^-$ can be measured and counted. The sensitivity toward X-H would be

521   reduced only when the first reversion pathway occurs to a non-negligible extent. Taking H$_2$SO$_4$ as an example, the

522   dissociation enthalpies for the first and second pathways are 41.1 and 27.9 kcal mol^{-1}, respectively. If some of the

523   H$_2$SO$_4$·Br$^-$ dissociate, they preferably become HSO$_4^-$ and are detectable by the Br-CIMS. Thus, H$_2$SO$_4$ can be detected

524   at the maximum sensitivity. ~~We list the cluster formation enthalpies for a selection of halogen containing species in~~

525   ~~Table 1 and the corresponding cluster dissociation enthalpies in Table 2.~~

526

527   While we were unable to experimentally establish a correlation between sensitivities and binding enthalpies due to

528   limited quantifiable halogen species, we can predict the tentative critical enthalpy as the binding enthalpy of a species

529   that is likely detected at the maximum sensitivity. We list the cluster formation enthalpies for a selection of halogen

530   containing species in Table 1 and the corresponding cluster dissociation enthalpies in Table 2. Among all the

531   calibration coefficients listed in Table 3, H$_2$SO$_4$ and I$_2$ have the lowest calibration coefficients (highest sensitivities)~~;~~

532   ~~and their coefficients are almost the same for both the online and offline calibrations, with discrepancies well within~~

533   ~~the systematic uncertainties~~. Thereby, we conclude that both H$_2$SO$_4$ and I$_2$ are detected at the maximum sensitivity,

534   suggesting a critical enthalpy not higher than 33.7 kcal mol^{-1}. We can then infer the sensitivity for other species that

535   are difficult to calibrate by comparing their binding enthalpies to those of the benchmark species. For example, ICl

536   and IBr should have the maximum sensitivity, since the dissociation enthalpies for ICl·Br$^-$ and IBr·Br$^-$ are both much

537   higher than 33.7 kcal mol^{-1} (Table 2). Although HIO$_3$·Br$^-$ has a lower dissociation enthalpy than the critical value, the

538   favored dissociation pathway is proton transfer (the second pathway); HIO$_3$ can thus be considered as a maximum

539   sensitivity species detectable as IO$_3^-$ ions after proton transfer. This is consistent with the fact that both HIO$_3$·Br$^-$ and

540   IO$_3^-$ are detected in Figure 1, so is the case with H$_2$SO$_4$. We thus assume that HIO$_3$ has a kinetic calibration coefficient

541   of 4.1×10^{10} molec cm^{-3} cps cps^{-1}, the value for H$_2$SO$_4$. However, the lowest dissociation enthalpies of HOI·Br$^-$ and

542   Cl$_2$·Br$^-$ are 26.9 and 22.3 kcal mol^{-1}, respectively, consistent with their higher calibration coefficients of 3.3×10^{11} and

543   3.5×10^{11} molec cm^{-3} cps cps^{-1}. The dissociation enthalpies for $IO \cdot Br^-$, $OIO \cdot Br^-$, and $HIO_2 \cdot Br^-$ are 24.5, 23.2, and 29.2

544   kcal mol^{-1}, respectively. We would expect that their sensitives are lower than the maximum sensitivity. Since the

545   dissociation enthalpies for $IO \cdot Br^-$ and $OIO \cdot Br^-$ are between those of $HOI \cdot Br^-$ and $Cl_2 \cdot Br^-$, a similar calibration

546   coefficient ~~of around 3.0×10^{11} molec cm^{-3} cps cps^{-1} could~~may be applied, but direct calibrations are more preferable.

547   We note that when transferring the calibration factor from one species to another, the diffusivity difference should be

548   accounted, since it affects the inlet line loss. This factor is not considered in the cluster enthalpies calculations.

549

550   Further, we estimate the detection limit of the calibrated species. The detection limit is defined as the analyte

551   concentration, corresponding to the sum of the mean signal and three times the standard deviations (3σ) of the

552   background fluctuations during a two-hour background measurement. We derive the detection limit of HOI, HIO_3, I_2,

553   and H_2SO_4 to be 5.8×10^6, 1.2×10^5, $3.8\underline{6.3} \times 10^5$, and 2.0×10^5 molec cm^{-3} (or 0.2, 0.005, 0.~~03~~015, and 0.008 pptv),

554   respectively, for a 2-min integration time.

555

556   **3.4 Comparison between Br-MION-CIMS and Br-FIGAERO-CIMS**

557   While Br-MION-CIMS and Br-FIGAERO-CIMS use the same chemical ionization scheme, their designs differ in the

558   ion-molecule reaction chamber (IMR). MION is an atmospheric pressure (1 bar) drift tube; analyte molecules gain an

559   electric charge in an axial laminar flow. FIGAERO is connected to a cone-shaped IMR chamber operated at a reduced

560   pressure (150 mbar); the sample flow is injected into the inlet via an orifice, necessarily causing turbulence and wall

561   interactions in the IMR region. The atmospheric pressure and reduced pressure IMRs are both widely used for trace

562   gas measurements. We thus compare iodine species measurements from Br-MION-CIMS and Br-FIGAERO-CIMS,

563   to better understand the performance and applicability of the bromide ionization scheme.

564

565   ~~**3.4.1 Signal trend and detection limit**~~

566   We show in Fig. 5 the same iodine oxidation ~~new particle formation~~ event as in Fig. 2, to illustrate the time series for

567      $HIO_3 \cdot Br^-$, $HOI \cdot Br^-$, $IO \cdot Br^-$, and $I_2 \cdot Br^-$, measured with Br-MION-CIMS (red circles) and Br-FIGAERO-CIMS (grey

568   sticks), respectively. Note that the FIGAERO alternates between gas and particle measurements; here we show only

569   the gas-phase signals. Clear and concurrent signals of HIO_3, HOI, IO, and I_2 are evident from both the Br-MION-

570   CIMS and Br-FIGAERO-CIMS. Prior to the ~~NPF~~ iodine oxidation event (08:11), there was no photochemical

571   production and thus virtually no signal of oxidized iodine species in both instruments. The dark reaction of ozone with

572   I_2 did not proceed at a significant rate, due to the low rate coefficient and to low levels of I_2. Signals detected during

573   this period are considered as the persistent background, coming from electronic noise or other sources such as the

574   ionizer, carrier flows, or long-term "memory" in the case of the Br-FIGAERO-CIMS. Not surprisingly, the Br-MION-

575   CIMS has a near-zero background for all analytes. For HIO_3 (Fig. 5 (a)), the background signal in the Br-FIGAERO-

576   CIMS is also negligible; however, IO shows a substantial persistent background (Fig. 5 (c)) in the Br-FIGAERO-

577   CIMS. ~~After the NPF event (10:21), the photochemical production of oxidized iodine species was terminated and~~

578   ~~vapor concentrations decayed exponentially due to dilution and losses to chamber walls. The I_2 signal increases after~~

579   ~~the event termination because it is no longer photolyzed.~~

580

581 When we initiated the photochemistry, oxidized iodine signals rapidly built up toward an asymptote within timescales

582 of minutes. The ~~HIO₃ signals rose with a time constant of 102 s in the Br-MION-CIMS and 108 s in the Br-FIGAERO-~~

583 ~~CIMS, both with t_{app} = ~ 300 s. The fitted time constants of HOI are slightly longer than those of HIO₃, with 120 s in~~

584 ~~the Br-MION-CIMS and 114 s in the Br-FIGAERO-CIMS. IO signals stabilized the earliest, thus have the fastest time~~

585 ~~constants of 48 s in the Br-MION-CIMS and 84 s in the Br-FIGAERO-CIMS. The~~ instrumental differences in these

586 timescales are small for HIO_3 and HOI, but larger for IO. When colliding with the IMR surface, HIO_3 condenses

587 irreversibly; it thus makes sense that the Br-MION-CIMS and Br-FIGAERO-CIMS signals show the same ~~time~~

588 ~~constant~~timescale for HIO_3. Semi-volatile HOI, however, can return to the gas phase from the walls depending on the

589 surface coverage of HOI and the vapor concentration. Additionally, the heterogeneous reaction of aqueous iodide (I⁻)

590 and ozone (Carpenter et al., 2013) could also contribute to the emission of HOI from the IMR wall in the FIGAERO.

591 As the evaporation flux is typically a function of the amount analyte on the surface, the buffering effect could degrade

592 the instrument time response upon changes in analyte concentration. Here, however, we did not observe a significant

593 memory effect, likely because the HOI concentration was too low to fully saturate the IMR surface or because any

594 HOI evaporation was suppressed due to an enhanced accommodation coefficient of HOI on the metal surface. We

595 expect IO to be prone to loss on the metal surface due to its radical nature.

596

597 After the iodine oxidation event (10:21), the photochemical production of oxidized iodine species was terminated and

598 vapor concentrations decayed exponentially due to dilution and losses to chamber walls. Memory effects could also

599 influence the signal time constant. The dilution loss rate was around 2.1×10^{-4} s⁻¹ (4760 s time constant) for all species

600 in the chamber, determined by the total chamber flow rate and the chamber volume. Wall loss rates, however, vary

601 for species with different diffusion constants. The decay rates of HIO_3 are 400 s for the Br-MION-CIMS and 370 s for

602 the Br-FIGAERO-CIMS, much faster than the dilution loss. For comparison, the time constant for H_2SO_4 vapor loss

603 was 300 s. These time constants are thus consistent with wall loss (around 2.2×10^{-3} s⁻¹). The IO decay time constant

604 is 294 s for the Br-MION-CIMS and 435 s for the Br-FIGAERO-CIMS. The time constant for the Br-MION-CIMS

605 indicates that the decay of IO is also driven by wall loss, so the net flux during this period was thus towards the wall

606 rather than from the wall. Therefore, the difference of IO between instruments may well be attributed to the persistent

607 background from the ionizer of the FIGAERO. The HOI signals have longer decay time constants in both instruments

608 of 909 s for the Br-MION-CIMS and 714 s for the Br-FIGAERO-CIMS; this may reflect a time constant for depletion

609 of HOI adsorbed to the chamber walls. The I_2 signal increases after the event termination because it is no longer

610 photolyzed while its injection continues.

611

612 Applying the calibration coefficients, we convert the Br-MION-CIMS signals to absolute concentrations, and

613 subsequently correlate them with signals measured with Br-FIGAERO-CIMS. We then estimate the tentative detection

614 limits for HOI and HIO_3 in the Br-FIGAERO-CIMS to be 3.3×10^7 and 5.1×10^6 molec cm⁻³ (versus 5.8×10^6 and 1.2×10^5

615 molec cm⁻³ in the Br-MION-CIMS), respectively, at 3σ of the background signal for a 2-min integration time during

616 a two-hour period; they are in general one order of magnitude higher than those in the Br-MION-CIMS. This is in line

617 with the higher background signals observed in the Br-FIGAERO-CIMS. Note that for both HOI and HIO$_3$ the
618 uncertainties introduced from the correlational analysis are negligible compared to the limited accuracy of the
619 calibration sources (55 % for HOI and +50/-33 % for HIO$_3$). We are unable to estimate the I$_2$ detection limit in the Br-
620 FIGAREO-CIMS, due to a lack of I$_2$ background measurement; but Br-FIGAERO-CIMS can and did detect I$_2$ at the
621 low pptv level with good fidelity.

622
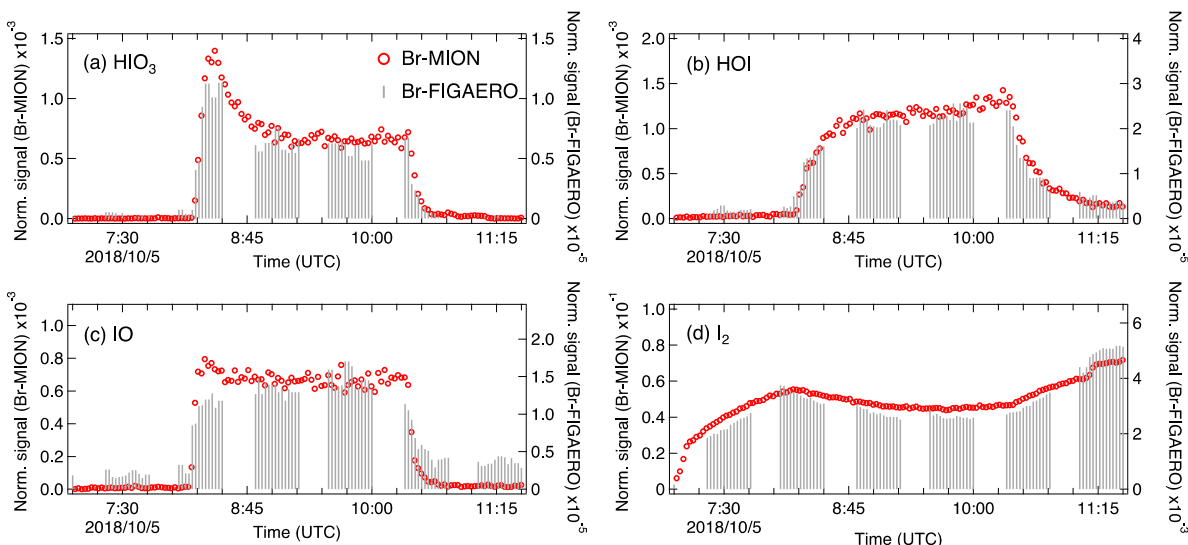
623
624 **Figure 5.** Signal comparison of selected iodine species measured with Br-MION-CIMS and (gas-phase) Br-FIGAERO-CIMS,
625 respectively, during the same iodine oxidation ~~new particle formation~~ experiment shown in Fig. 2.
626

627 ~~**3.4.2 Rise and decay time constants**~~

628 ~~In order to quantitatively compare the performance of the two types of IMRs, we set the initiation (08:11) and~~
629 ~~termination (10:21) of NPF event as $t = 0$, and fit the rise and decay rates of HIO$_3$, HOI and IO in both instruments,~~
630 ~~respectively.~~

631

632 ~~When we initiated the photochemistry, oxidized iodine species rapidly built up toward an asymptote; we thus fit their~~
633 ~~time series signals individually with a four-parameter sigmoid function using a least-squares fitting algorithm:~~

634 $$S_t(t) = a + (b - a)/\left(1 + e^{(-(t-t_{app})/c)}\right) \qquad (3)$$

635 ~~where a and b represent the background and asymptotic value of the sigmoid function respectively, c is the exponential~~
636 ~~time constant of the signal change, and t_{app} is the time at which the 50 % value between plateau and background is~~
637 ~~reached (50 % appearance time). As we were unable to separate the time scale of chemical reactions from that of~~
638 ~~instrument response, we use the time constants to represent the overall response for the purpose of comparing~~
639 ~~instrument performance.~~

640

641 ~~We show in Fig. 6 (a), (c), and (e) the rise rate fits of HIO$_3$, HOI, and IO, respectively.~~ ~~HIO$_3$ signals rose with a time~~
642 ~~constant of 102 s in the Br-MION-CIMS and 108 s in the Br-FIGAERO-CIMS, both with $t_{app} = -300$ s. The fitted time~~
643 ~~constants of HOI are slightly longer than those of HIO$_3$, with 120 s in the Br-MION-CIMS and 114 s in the Br-~~

FIGAERO-CIMS. IO signals stabilized the earliest, thus have the fastest time constants of 48 s in the Br-MION-CIMS and 84 s in the Br-FIGAERO-CIMS. The instrumental differences are small for HIO_3 and HOI, but larger for IO. When colliding with the IMR surface, HIO_3 condenses irreversibly; it thus makes sense that the Br-MION-CIMS and Br-FIGAERO-CIMS signals show the same time constant for HIO_3. Semi-volatile HOI, however, can return to the gas phase from the walls depending on the surface coverage of HOI and the vapor concentration. Additionally, the heterogeneous reaction of aqueous iodide (I^-) and ozone (Carpenter et al., 2013) could also contribute to the emission of HOI from the IMR wall in the FIGAERO. As the evaporation flux is typically a function of the amount analyte on the surface, the buffering effect could degrade the instrument time response upon changes in analyte concentration. Here, however, we did not observe a significant memory effect, likely because the HOI concentration was too low to fully saturate the IMR surface or because any HOI evaporation was suppressed due to an enhanced accommodation coefficient of HOI on the metal surface. We expect IO to be prone to loss on the metal surface due to its radical nature.

We also fit the exponential decay time constants of these iodine species to test this interpretation (Fig. 6 (b), (d), and (f)). After photochemistry was terminated at the end of the NPF event, only two sinks drove the vapor concentration decay – dilution and wall loss. Memory effects could also influence the signal time constant. The dilution loss rate was around 2.1×10^{-4} s^{-1} (4760 s time constant) for all species in the chamber, determined by the total chamber flow rate and the chamber volume. Wall loss rates, however, vary for species with different diffusion constants. The decay rates of HIO_3 are 400 s for the Br-MION-CIMS and 370 s for the Br-FIGAERO-CIMS, much faster than the dilution loss. For comparison, the time constant for H_2SO_4 vapor loss was 300 s. These time constants are thus consistent with wall loss (around 2.2×10^{-3} s^{-1}). The IO decay time constant is 294 s for the Br-MION-CIMS and 435 s for the Br-FIGAERO-CIMS. The time constant for the Br-MION-CIMS indicates that the decay of IO is also driven by wall loss, so the net flux during this period was thus towards the wall rather than from the wall. Therefore, the difference of IO between instruments may well be attributed to the persistent background from the ionizer of the FIGAERO. The HOI signals have longer decay time constants in both instruments of 909 s for the Br-MION-CIMS and 714 s for the Br-FIGAERO-CIMS; this may reflect a time constant for depletion of HOI adsorbed to the chamber walls.
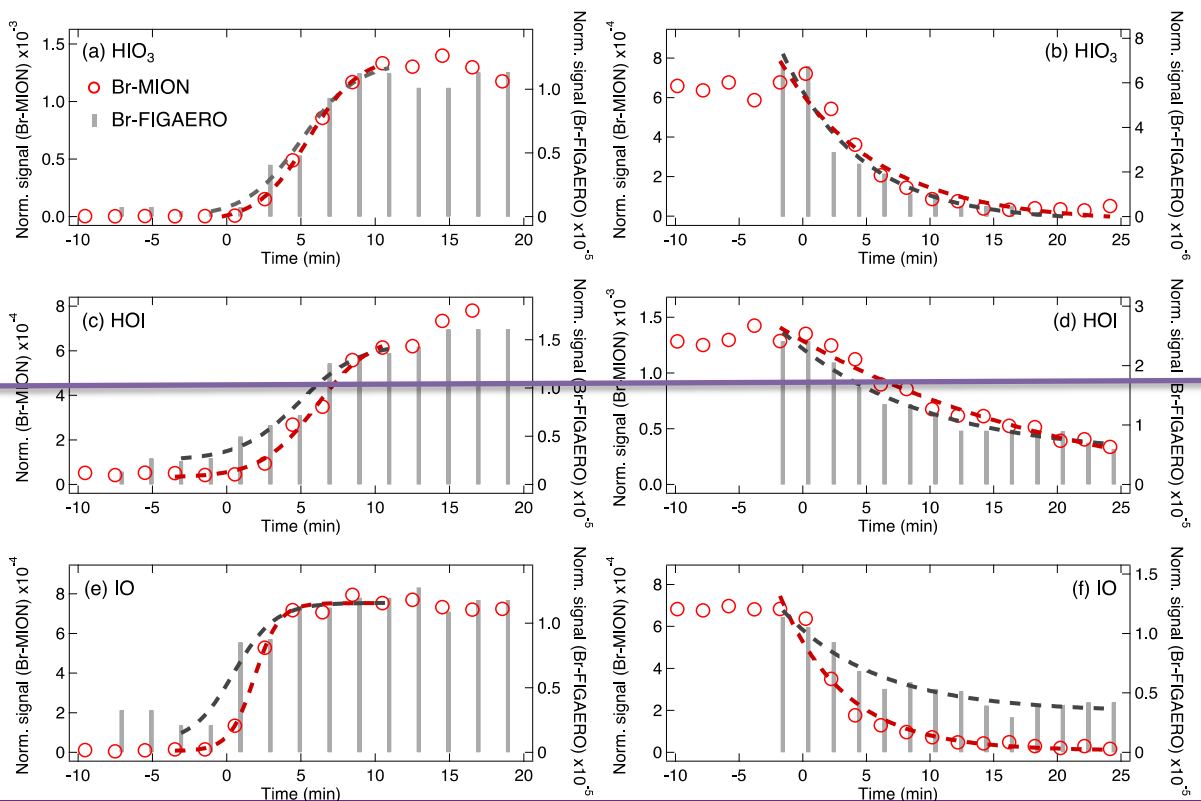
4 Summary and conclusion

We confirm in this study that bromide chemical ionization is a suitable technique for the time-resolved, highly sensitive, and simultaneous measurements of iodine species and sulfuric acid. The Br-MION-CIMS shows constant sensitivity throughout the relative humidity range of 40 to 80 % at -10 °C, as long as the sum of the two reagent ions (Br^- + $H_2O \cdot Br^-$) is used for signal normalization. This demonstrates the applicability of this technique to field measurements in the ambient marine environment.

We quantify iodine species and sulfuric acid via offline calibrations (i.e. permeation tube and calibrator) and inter-method calibrations (i.e. CE-DOAS and pre-calibrated nitrate-CIMS~~); different methods result in consistent calibration coefficients~~. Further, we calculate the binding enthalpies between the calibrated species and reagent ions, which qualitatively agree with the corresponding calibration coefficients. This indicates that the quantum chemical calculations can be employed along with the calibration experiments to determine the sensitivities for unquantifiable species; more work is required to further establish the correlation between calibration coefficients and binding enthalpies.

Further, using inter-method and offline calibrations, we estimate the detection limits of HOI, HIO_3, I_2, and H_2SO_4 in Br-MION-CIMS being 5.8×10^6, 1.2×10^5, 3.8~~6.3~~$\times 10^5$, and 2.0×10^5 molec cm^{-3}, respectively, for a 2-min integration time during a two-hour period. To our knowledge, the simultaneous measurements of various iodine species and

24

692 sulfuric acid with low detection limits are unprecedented for online techniques. Detection limits for HOI and HIO_3 in

693 the Br-FIGAERO-CIMS are 3.3×10^7 and 5.1×10^6 molec cm^{-3}, which are in general one order of magnitude higher than

694 those in the Br-MION-CIMS. The signal comparison between the two instruments also shows that the Br-CIMS can

695 be coupled to both the atmospheric pressure and the reduced pressure interfaces for iodine species and sulfuric acid

696 measurements in the marine environment.

697

698

720

721 **References**

722 Bitter, M., Ball, S. M., Povey, I. M. and Jones, R. L.: A broadband cavity ringdown spectrometer for in-situ

723 measurements of atmospheric trace gases, Atmos. Chem. Phys., doi:10.5194/acp-5-2547-2005, 2005.

724 Carpenter, L. J., MacDonald, S. M., Shaw, M. D., Kumar, R., Saunders, R. W., Parthipan, R., Wilson, J. and Plane,

725 J. M. C.: Atmospheric iodine levels influenced by sea surface emissions of inorganic iodine, Nat. Geosci.,

726 doi:10.1038/ngeo1687, 2013.

727 Chai, J. Da and Head-Gordon, M.: Long-range corrected hybrid density functionals with damped atom-atom

728 dispersion corrections, Phys. Chem. Chem. Phys., doi:10.1039/b810189b, 2008.

729 Chance, R. J., Shaw, M., Telgmann, L., Baxter, M. and Carpenter, L. J.: A comparison of spectrophotometric and

730 denuder based approaches for the determination of gaseous molecular iodine, Atmos. Meas. Tech., doi:10.5194/amt-

731 3-177-2010, 2010.

732 Dias, A., Ehrhart, S., Vogel, A., Mathot, S., Onnela, A., Almeida, J., Kirkby, J., Williamson, C. and Mumford, S.:

733 Temperature uniformity in the CERN CLOUD chamber, Atmos. Meas. Tech., 10, 5075–5088, 2017.

734 Dillon, T. J., Tucceri, M. E. and Crowley, J. N.: Laser induced fluorescence studies of iodine oxide chemistry: Part

735 II. The reactions of IO with CH3O2, CF3O2 and O3, Phys. Chem. Chem. Phys., doi:10.1039/b611116e, 2006.

736 Duplissy, J., Merikanto, J., Franchin, A., Tsagkogeorgas, G., Kangasluoma, J., Wimmer, D., Vuollekoski, H.,

737 Schobesberger, S., Lehtipalo, K., Flagan, R. C., Brus, D., Donahue, N. M., Vehkamaki, H., Almeida, J., Amorim,
738 A., Barmet, P., Bianchi, F., Breitenlechner, M., Dunne, E. M., Guida, R., Henschel, H., Junninen, H., Kirkby, J.,
739 Kurten, A., Kupc, A., Maattanen, A., Makhmutov, V., Mathot, S., Nieminen, T., Onnela, A., Praplan, A. P.,
740 Riccobono, F., Rondo, L., Steiner, G., Tome, A., Walther, H., Baltensperger, U., Carslaw, K. S., Dommen, J.,
741 Hansel, A., Petaja, T., Sipila, M., Stratmann, F., Vrtala, A., Wagner, P. E., Worsnop, D. R., Curtius, J. and Kulmala,
742 M.: Effect of ions on sulfuric acid-water binary particle formation: 2. Experimental data and comparison with QC-
743 normalized classical nucleation theory, J. Geophys. Res., 121, 1752–1775, doi:10.1002/2015JD023539, 2016.

744 Feller, D.: The role of databases in support of computational chemistry calculations, J. Comput. Chem.,
745 doi:10.1002/(SICI)1096-987X(199610)17:13<1571::AID-JCC9>3.0.CO;2-P, 1996.

746 Finley, B. D. and Saltzman, E. S.: Observations of Cl2, Br2, and I2 in coastal marine air, J. Geophys. Res. Atmos.,
747 doi:10.1029/2008JD010269, 2008.

748 Frisch, M. J., Trucks, G. W., Schlegel, H. B., Scuseria, G. E., Robb, M. A., Cheeseman, J. R., Scalmani, G., Barone,
749 V., Mennucci, B., Petersson, G. A., Nakatsuji, H., Caricato, M., Li, X., Hratchian, H. P., Izmaylov, A. F., Bloino, J.,
750 Zheng, G., Sonnenberg, J. L., Hada, M., Ehara, M., Toyota, K., Fukuda, R., Hasegawa, J., Ishida, M., Nakajima, T.,
751 Honda, Y., Kitao, O., Nakai, H., Vreven, T., Montgomery Jr., J. A., Peralta, J. E., Ogliaro, F., Bearpark, M., Heyd, J.
752 J., Brothers, E., Kudin, K. N., Staroverov, V. N., Kobayashi, R., Normand, J., Raghavachari, K., Rendell, A.,
753 Burant, J. C., Iyengar, S. S., Tomasi, J., Cossi, M., Rega, N., Millam, J. M., Klene, M., Knox, J. E., Cross, J. B.,
754 Bakken, V., Adamo, C., Jaramillo, J., Gomperts, R., Stratmann, R. E., Yazyev, O., Austin, A. J., Cammi, R.,
755 Pomelli, C., Ochterski, J. W., Martin, R. L., Morokuma, K., Zakrzewski, V. G., Voth, G. A., Salvador, P.,
756 Dannenberg, J. J., Dapprich, S., Daniels, A. D., Farkas, �., Foresman, J. B., Ortiz, J. V, Cioslowski, J. and Fox, D.
757 J.: Gaussian09 Revision D.01, Gaussian Inc. Wallingford CT, Gaussian 09 Revis. C.01, 2010.

758 Gallagher, M. S., King, D. B., Whung, P. Y. and Saltzman, E. S.: Performance of the HPLC/fluorescence SO2
759 detector during the GASIE instrument intercomparison experiment, J. Geophys. Res. Atmos.,
760 doi:10.1029/97jd00700, 1997.

761 Gómez Martín, J. C., Blahins, J., Gross, U., Ingham, T., Goddard, A., Mahajan, A. S., Ubelis, A. and Saiz-Lopez,
762 A.: In situ detection of atomic and molecular iodine using Resonance and Off-Resonance Fluorescence by Lamp
763 Excitation: ROFLEX, Atmos. Meas. Tech., doi:10.5194/amt-4-29-2011, 2011.

764 Gómez Martín, J. C., Gálvez, O., Baeza-Romero, M. T., Ingham, T., Plane, J. M. C. and Blitz, M. A.: On the
765 mechanism of iodine oxide particle formation, Phys. Chem. Chem. Phys., doi:10.1039/c3cp51217g, 2013.

766 He, X.-C., Iyer, S., Sipilä, M., Ylisirniö, A., Peltola, M., Kontkanen, J., Baalbaki, R., Simon, M., Kürten, A., Tham,
767 Y. J., Pesonen, J., Ahonen, L. R., Amanatidis, S., Amorim, A., Baccarini, A., Beck, L., Bianchi, F., Brilke, S., Chen,
768 D., Chiu, R., Curtius, J., Dada, L., Dias, A., Dommen, J., Donahue, N. M., Duplissy, J., El Haddad, I., Finkenzeller,
769 H., Fischer, L., Heinritzi, M., Hofbauer, V., Kangasluoma, J., Kim, C., Koenig, T. K., Kubečka, J., Kvashnin, A.,
770 Lamkaddam, H., Lee, C. P., Leiminger, M., Li, Z., Makhmutov, V., Xiao, M., Marten, R., Nie, W., Onnela, A.,
771 Partoll, E., Petäjä, T., Salo, V.-T., Schuchmann, S., Steiner, G., Stolzenburg, D., Stozhkov, Y., Tauber, C., Tomé,
772 A., Väisänen, O., Vazquez-Pufleau, M., Volkamer, R., Wagner, A. C., Wang, M., Wang, Y., Wimmer, D., Winkler,
773 P. M., Worsnop, D. R., Wu, Y., Yan, C., Ye, Q., Lehtinen, K., Nieminen, T., Manninen, H. E., Rissanen, M.,
774 Schobesberger, S., Lehtipalo, K., Baltensperger, U., Hansel, A., Kerminen, V.-M., Flagan, R. C., Kirkby, J., Kurtén,
775 T. and Kulmala, M.: Determination of the collision rate coefficient between charged iodic acid clusters and iodic
776 acid using the appearance time method, Aerosol Sci. Technol., 55(2), 231–242,
777 doi:10.1080/02786826.2020.1839013, 2021a.

778 He, X.-C., Tham, Y. J., Dada, L., Wang, M., Finkenzeller, H., Stolzenburg, D., Iyer, S., Simon, M., Kürten, A.,
779 Shen, J. and others: Role of iodine oxoacids in atmospheric aerosol nucleation, Science (80-.)., 371(6529), 589–
780 595, 2021b.

781 He, X.: From the measurement of halogenated species to iodine particle formation, 2017.

782 Iyer, S., Lopez-Hilfiker, F., Lee, B. H., Thornton, J. A. and Kurtén, T.: Modeling the Detection of Organic and
783 Inorganic Compounds Using Iodide-Based Chemical Ionization, J. Phys. Chem. A, doi:10.1021/acs.jpca.5b09837,
784 2016.

785 Junninen, H., Ehn, M., Petaja, T., Luosujarvi, L., Kotiaho, T., Kostiainen, R., Rohner, U., Gonin, M., Fuhrer, K.,
786 Kulmala, M., Worsnop, D. R., Petäjä, T., Luosujärvi, L., Kotiaho, T., Kostiainen, R., Rohner, U., Gonin, M., Fuhrer,

787 K., Kulmala, M. and Worsnop, D. R.: A high-resolution mass spectrometer to measure atmospheric ion composition,
788 Atmos. Meas. Tech., 3(4), 1039–1053, doi:10.5194/amt-3-1039-2010, 2010.

789 Kazantseva, N. N., Ernepesova, A., Khodjamamedov, A., Geldyev, O. A. and Krumgalz, B. S.: Spectrophotometric
790 analysis of iodide oxidation by chlorine in highly mineralized solutions, in Analytica Chimica Acta., 2002.

791 Kendall, R. A., Dunning, T. H. and Harrison, R. J.: Electron affinities of the first-row atoms revisited. Systematic
792 basis sets and wave functions, J. Chem. Phys., doi:10.1063/1.462569, 1992.

793 Kercher, J. P., Riedel, T. P. and Thornton, J. A.: Chlorine activation by N2O5: Simultaneous, in situ detection of
794 ClNO2 and N2O5 by chemical ionization mass spectrometry, Atmos. Meas. Tech., doi:10.5194/amt-2-193-2009,
795 2009.

796 Kirkby, J., Curtius, J., Almeida, J., Dunne, E., Duplissy, J., Ehrhart, S., Franchin, A., Gagné, S., Ickes, L., Kürten,
797 A., Kupc, A., Metzger, A., Riccobono, F., Rondo, L., Schobesberger, S., Tsagkogeorgas, G., Wimmer, D., Amorim,
798 A., Bianchi, F., Breitenlechner, M., David, A., Dommen, J., Downard, A., Ehn, M., Flagan, R. C., Haider, S.,
799 Hansel, A., Hauser, D., Jud, W., Junninen, H., Kreissl, F., Kvashin, A., Laaksonen, A., Lehtipalo, K., Lima, J.,
800 Lovejoy, E. R., Makhmutov, V., Mathot, S., Mikkilä, J., Minginette, P., Mogo, S., Nieminen, T., Onnela, A.,
801 Pereira, P., Petäjä, T., Schnitzhofer, R., Seinfeld, J. H., Sipilä, M., Stozhkov, Y., Stratmann, F., Tomé, A.,
802 Vanhanen, J., Viisanen, Y., Vrtala, A., Wagner, P. E., Walther, H., Weingartner, E., Wex, H., Winkler, P. M.,
803 Carslaw, K. S., Worsnop, D. R., Baltensperger, U. and Kulmala, M.: Role of sulphuric acid, ammonia and galactic
804 cosmic rays in atmospheric aerosol nucleation, Nature, 476, 429 [online] Available from:
805 https://doi.org/10.1038/nature10343, 2011.

806 Kirkby, J., Duplissy, J., Sengupta, K., Frege, C., Gordon, H., Williamson, C., Heinritzi, M., Simon, M., Yan, C.,
807 Almeida, J., Trostl, J., Nieminen, T., Ortega, I. K., Wagner, R., Adamov, A., Amorim, A., Bernhammer, A. K.,
808 Bianchi, F., Breitenlechner, M., Brilke, S., Chen, X. M., Craven, J., Dias, A., Ehrhart, S., Flagan, R. C., Franchin,
809 A., Fuchs, C., Guida, R., Hakala, J., Hoyle, C. R., Jokinen, T., Junninen, H., Kangasluoma, J., Kim, J., Krapf, M.,
810 Kurten, A., Laaksonen, A., Lehtipalo, K., Makhmutov, V., Mathot, S., Molteni, U., Onnela, A., Perakyla, O., Piel,
811 F., Petaja, T., Praplan, A. P., Pringle, K., Rap, A., Richards, N. A. D. D., Riipinen, I., Rissanen, M. P., Rondo, L.,
812 Sarnela, N., Schobesberger, S., Scott, C. E., Seinfeld, J. H., Sipila, M., Steiner, G., Stozhkov, Y., Stratmann, F.,
813 Tome, A., Virtanen, A., Vogel, A. L., Wagner, A. C., Wagner, P. E., Weingartner, E., Wimmer, D., Winkler, P. M.,
814 Ye, P. L., Zhang, X., Hansel, A., Dommen, J., Donahue, N. M., Worsnop, D. R., Baltensperger, U., Kulmala, M.,
815 Carslaw, K. S., Curtius, J., Tomé, A., Virtanen, A., Vogel, A. L., Wagner, A. C., Wagner, P. E., Weingartner, E.,
816 Wimmer, D., Winkler, P. M., Ye, P. L., Zhang, X., Hansel, A., Dommen, J., Donahue, N. M., Worsnop, D. R.,
817 Baltensperger, U., Kulmala, M., Carslaw, K. S. and Curtius, J.: Ion-induced nucleation of pure biogenic particles,
818 Nature, 533(7604), 521–526, doi:10.1038/nature17953, 2016.

819 Koenig, T. K., Baidar, S., Campuzano-Jost, P., Cuevas, C. A., Dix, B., Fernandez, R. P., Guo, H., Hall, S. R.,
820 Kinnison, D., Nault, B. A., Ullmann, K., Jimenez, J. L., Saiz-Lopez, A. and Volkamer, R.: Quantitative detection of
821 iodine in the stratosphere, Proc. Natl. Acad. Sci. U. S. A., doi:10.1073/pnas.1916828117, 2020.

822 Kurten, A., Rondo, L., Ehrhart, S. and Curtius, J.: Calibration of a Chemical Ionization Mass Spectrometer for the
823 Measurement of Gaseous Sulfuric Acid, J. Phys. Chem. A, 116, 6375–6386, doi:Doi 10.1021/Jp212123n, 2012.

824 Lawler, M. J., Sander, R., Carpenter, L. J., Lee, J. D., Von Glasow, R., Sommariva, R. and Saltzman, E. S.: HOCl
825 and Cl2 observations in marine air, Atmos. Chem. Phys., doi:10.5194/acp-11-7617-2011, 2011.

826 Lee, B. H., Lopez-Hilfiker, F. D., Mohr, C., Kurten, T., Worsnop, D. R. and Thornton, J. A.: An iodide-adduct high-
827 resolution time-of-flight chemical-ionization mass spectrometer: application to atmospheric inorganic and organic
828 compounds, Env. Sci Technol, 48(11), 6309–6317, doi:10.1021/es500362a, 2014.

829 Lee, B. H., Lopez-Hilfiker, F. D., Veres, P. R., McDuffie, E. E., Fibiger, D. L., Sparks, T. L., Ebben, C. J., Green, J.
830 R., Schroder, J. C., Campuzano-Jost, P., Iyer, S., D'Ambro, E. L., Schobesberger, S., Brown, S. S., Wooldridge, P.
831 J., Cohen, R. C., Fiddler, M. N., Bililign, S., Jimenez, J. L., Kurtén, T., Weinheimer, A. J., Jaegle, L. and Thornton,
832 J. A.: Flight Deployment of a High-Resolution Time-of-Flight Chemical Ionization Mass Spectrometer:
833 Observations of Reactive Halogen and Nitrogen Oxide Species, J. Geophys. Res. Atmos.,
834 doi:10.1029/2017JD028082, 2018.

835 Leigh, R. J., Ball, S. M., Whitehead, J., Leblanc, C., Shillings, A. J. L., Mahajan, A. S., Oetjen, H., Lee, J. D., Jones,
836 C. E., Dorsey, J. R., Gallagher, M., Jones, R. L., Plane, J. M. C., Potin, P. and McFiggans, G.: Measurements and

837   modelling of molecular iodine emissions, transport and photodestruction in the coastal region around Roscoff,
838   Atmos. Chem. Phys., doi:10.5194/acp-10-11823-2010, 2010.

839   Lopez-Hilfiker, F. D., Mohr, C., Ehn, M., Rubach, F., Kleist, E., Wildt, J., Mentel, T. F., Lutz, A., Hallquist, M.,
840   Worsnop, D. and Thornton, J. A.: A novel method for online analysis of gas and particle composition: description
841   and evaluation of a Filter Inlet for Gases and AEROsols (FIGAERO), Atmos. Meas. Tech., 7(4), 983–1001,
842   doi:10.5194/amt-7-983-2014, 2014.

843   Lopez-Hilfiker, F. D., Iyer, S., Mohr, C., Lee, B. H., D'ambro, E. L., Kurtén, T. and Thornton, J. A.: Constraining
844   the sensitivity of iodide adduct chemical ionization mass spectrometry to multifunctional organic molecules using
845   the collision limit and thermodynamic stability of iodide ion adducts, Atmos. Meas. Tech., doi:10.5194/amt-9-1505-
846   2016, 2016.

847   Marcy, T. P., Fahey, D. W., Gao, R. S., Popp, P. J., Richard, E. C., Thompson, T. L., Rosenlof, K. H., Ray, E. A.,
848   Salawitch, R. J., Atherton, C. S., Bergmann, D. J., Ridley, B. A., Weinheimer, A. J., Loewenstein, M., Weinstock, E.
849   M. and Mahoney, M. J.: Quantifying Stratospheric Ozone in the Upper Troposphere with in Situ Measurements of
850   HCl, Science (80-.)., doi:10.1126/science.1093418, 2004.

851   McFiggans, G., Coe, H., Burgess, R., Allan, J., Cubison, M., Alfarra, M. R., Saunders, R., Saiz-Lopez, A., Plane, J.
852   M. C., Wevill, D. J., Carpenter, L. J., Rickard, A. R. and Monks, P. S.: Direct evidence for coastal iodine particles
853   from Laminaria macroalgae - Linkage to emissions of molecular iodine, Atmos. Chem. Phys., doi:10.5194/acp-4-
854   701-2004, 2004.

855   Meinen, J., Thieser, J., Platt, U. and Leisner, T.: Technical Note: Using a high finesse optical resonator to provide a
856   long light path for differential optical absorption spectroscopy: CE-DOAS, Atmos. Chem. Phys., doi:10.5194/acp-
857   10-3901-2010, 2010.

858   Neese, F.: The ORCA program system, Wiley Interdiscip. Rev. Comput. Mol. Sci., doi:10.1002/wcms.81, 2012.

859   O'dowd, C. D., Jimenez, J. L., Bahreini, R., Flagan, R. C., Seinfeld, J. H., Hämerl, K., Pirjola, L., Kulmala, M. and
860   Hoffmann, T.: Marine aerosol formation from biogenic iodine emissions, Nature, doi:10.1038/nature00775, 2002.

861   Passananti, M., Zapadinsky, E., Zanca, T., Kangasluoma, J., Myllys, N., Rissanen, M. P., Kurtén, T., Ehn, M.,
862   Attoui, M. and Vehkamäki, H.: How well can we predict cluster fragmentation inside a mass spectrometer?, Chem.
863   Commun., doi:10.1039/c9cc02896j, 2019.

864   Pfeifer, J., Simon, M., Heinritzi, M., Piel, F., Weitz, L., Wang, D., Granzin, M., Müller, T., Bräkling, S., Kirkby, J.,
865   Curtius, J. and Kürten, A.: Measurement of ammonia, amines and iodine compounds using protonated water cluster
866   chemical ionization mass spectrometry, Atmos. Meas. Tech., doi:10.5194/amt-13-2501-2020, 2020.

867   Prados-Roman, C., Cuevas, C. A., Fernandez, R. P., Kinnison, D. E., Lamarque, J. F. and Saiz-Lopez, A.: A
868   negative feedback between anthropogenic ozone pollution and enhanced ocean emissions of iodine, Atmos. Chem.
869   Phys., doi:10.5194/acp-15-2215-2015, 2015.

870   Raso, A. R. W., Custard, K. D., May, N. W., Tanner, D., Newburn, M. K., Walker, L., Moore, R. J., Huey, L. G.,
871   Alexander, L., Shepson, P. B. and Pratt, K. A.: Active molecular iodine photochemistry in the Arctic, Proc. Natl.
872   Acad. Sci. U. S. A., doi:10.1073/pnas.1702803114, 2017.

873   Riplinger, C. and Neese, F.: An efficient and near linear scaling pair natural orbital based local coupled cluster
874   method, J. Chem. Phys., doi:10.1063/1.4773581, 2013.

875   Rissanen, M. P., Mikkilä, J., Iyer, S. and Hakala, J.: Multi-scheme chemical ionization inlet (MION) for fast
876   switching of reagent ion chemistry in atmospheric pressure chemical ionization mass spectrometry (CIMS)
877   applications, Atmos. Meas. Tech., doi:10.5194/amt-12-6635-2019, 2019.

878   Rothman, L. S., Gordon, I. E., Barber, R. J., Dothe, H., Gamache, R. R., Goldman, A., Perevalov, V. I., Tashkun, S.
879   A. and Tennyson, J.: HITEMP, the high-temperature molecular spectroscopic database, J. Quant. Spectrosc. Radiat.
880   Transf., doi:10.1016/j.jqsrt.2010.05.001, 2010.

881   Saiz-Lopez, A., Plane, J. M. C., Baker, A. R., Carpenter, L. J., Von Glasow, R., Gómez Martín, J. C., McFiggans, G.
882   and Saunders, R. W.: Atmospheric chemistry of iodine, Chem. Rev., doi:10.1021/cr200029u, 2012.

883   Sanchez, J., Tanner, D. J., Chen, D., Huey, L. G. and Ng, N. L.: A new technique for the direct detection of HO2
884   radicals using bromide chemical ionization mass spectrometry (Br-CIMS): Initial characterization, Atmos. Meas.

885   Tech., doi:10.5194/amt-9-3851-2016, 2016.

886   Schnitzhofer, R., Metzger, A., Breitenlechner, M., Jud, W., Heinritzi, M., De Menezes, L.-P., Duplissy, J., Guida,
887   R., Haider, S., Kirkby, J. and others: Characterisation of organic contaminants in the CLOUD chamber at CERN,
888   Atmos. Meas. Tech., 7(7), 2159–2168, 2014.

889   Schwehr, K. A., Santschi, P. H. and Elmore, D.: The dissolved organic iodine species of the isotopic ratio of
890   129I/127I: A novel tool for tracing terrestrial organic carbon in the estuarine surface waters of Galveston Bay,
891   Texas, Limnol. Oceanogr. Methods, doi:10.4319/lom.2005.3.326, 2005.

892   Sherwen, T., Evans, M. J., Carpenter, L. J., Andrews, S. J., Lidster, R. T., Dix, B., Koenig, T. K., Sinreich, R.,
893   Ortega, I., Volkamer, R., Saiz-Lopez, A., Prados-Roman, C., Mahajan, A. S. and Ordóñez, C.: Iodine's impact on
894   tropospheric oxidants: A global model study in GEOS-Chem, Atmos. Chem. Phys., doi:10.5194/acp-16-1161-2016,
895   2016.

896   Simpson, W. R., Brown, S. S., Saiz-Lopez, A., Thornton, J. A. and Von Glasow, R.: Tropospheric Halogen
897   Chemistry: Sources, Cycling, and Impacts, Chem. Rev., doi:10.1021/cr5006638, 2015.

898   Sipilä, M., Sarnela, N., Jokinen, T., Henschel, H., Junninen, H., Kontkanen, J., Richters, S., Kangasluoma, J.,
899   Franchin, A., Peräkylä, O., Rissanen, M. P., Ehn, M., Vehkamäki, H., Kurten, T., Berndt, T., Petäjä, T., Worsnop,
900   D., Ceburnis, D., Kerminen, V. M., Kulmala, M. and O'Dowd, C.: Molecular-scale evidence of aerosol particle
901   formation via sequential addition of HIO3, Nature, doi:10.1038/nature19314, 2016.

902   Spietz, P., Martín, J. G. and Burrows, J. P.: Effects of column density on i2 spectroscopy and a determination of i2
903   absorption cross section at 500 nm, Atmos. Chem. Phys., doi:10.5194/acp-6-2177-2006, 2006.

904   Spolaor, A., Gabrieli, J., Martma, T., Kohler, J., Björkman, M. B., Isaksson, E., Varin, C., Vallelonga, P., Plane, J.
905   M. C. and Barbante, C.: Sea ice dynamics influence halogen deposition to Svalbard, Cryosphere, doi:10.5194/tc-7-
906   1645-2013, 2013.

907   Stolzenburg, D., Simon, M., Ranjithkumar, A., Kürten, A., Lehtipalo, K., Gordon, H., Ehrhart, S., Finkenzeller, H.,
908   Pichelstorfer, L., Nieminen, T. and others: Enhanced growth rate of atmospheric particles from sulfuric acid, Atmos.
909   Chem. Phys., 20(12), 7359–7372, 2020.

910   Thalman, R. and Volkamer, R.: Temperature dependent absorption cross-sections of O2-O 2 collision pairs between
911   340 and 630 nm and at atmospherically relevant pressure, Phys. Chem. Chem. Phys., doi:10.1039/c3cp50968k,
912   2013.

913   Tham, Y. J., Wang, Z., Li, Q., Yun, H., Wang, W., Wang, X., Xue, L., Lu, K., Ma, N., Bohn, B., Li, X., Kecorius,
914   S., Größ, J., Shao, M., Wiedensohler, A., Zhang, Y. and Wang, T.: Significant concentrations of nitryl chloride
915   sustained in the morning: Investigations of the causes and impacts on ozone production in a polluted region of
916   northern China, Atmos. Chem. Phys., doi:10.5194/acp-16-14959-2016, 2016.

917   Tham, Y. J., He, X.-C., Li, Q., Cuevas, C. A., Shen, J., Kalliokoski, J., Yan, C., Iyer, S., Lehmusjärvi, T., Jang, S.
918   and others: Direct field evidence of autocatalytic iodine release from atmospheric aerosol, Proc. Natl. Acad. Sci.,
919   118(4), 2021.

920   Vandaele, A. C., Hermans, C., Simon, P. C., Carleer, M., Colin, R., Fally, S., Mérienne, M. F., Jenouvrier, A. and
921   Coquart, B.: Measurements of the NO2 absorption cross-section from 42 000 cm-1 to 10 000 cm-1 (238-1000 nm) at
922   220 K and 294 K, J. Quant. Spectrosc. Radiat. Transf., doi:10.1016/S0022-4073(97)00168-4, 1998.

923   Vaughan, S., Gherman, T., Ruth, A. A. and Orphal, J.: Incoherent broad-band cavity-enhanced absorption
924   spectroscopy of the marine boundary layer species I2, IO and OIO, Phys. Chem. Chem. Phys.,
925   doi:10.1039/b802618a, 2008.

926   Wang, M., Kong, W., Marten, R., He, X. C., Chen, D., Pfeifer, J., Heitto, A., Kontkanen, J., Dada, L., Kürten, A.,
927   Yli-Juuti, T., Manninen, H. E., Amanatidis, S., Amorim, A., Baalbaki, R., Baccarini, A., Bell, D. M., Bertozzi, B.,
928   Bräkling, S., Brilke, S., Murillo, L. C., Chiu, R., Chu, B., De Menezes, L. P., Duplissy, J., Finkenzeller, H.,
929   Carracedo, L. G., Granzin, M., Guida, R., Hansel, A., Hofbauer, V., Krechmer, J., Lehtipalo, K., Lamkaddam, H.,
930   Lampimäki, M., Lee, C. P., Makhmutov, V., Marie, G., Mathot, S., Mauldin, R. L., Mentler, B., Müller, T., Onnela,
931   A., Partoll, E., Petäjä, T., Philippov, M., Pospisilova, V., Ranjithkumar, A., Rissanen, M., Rörup, B., Scholz, W.,
932   Shen, J., Simon, M., Sipilä, M., Steiner, G., Stolzenburg, D., Tham, Y. J., Tomé, A., Wagner, A. C., Wang, D. S.,
933   Wang, Y., Weber, S. K., Winkler, P. M., Wlasits, P. J., Wu, Y., Xiao, M., Ye, Q., Zauner-Wieczorek, M., Zhou, X.,

934 Volkamer, R., Riipinen, I., Dommen, J., Curtius, J., Baltensperger, U., Kulmala, M., Worsnop, D. R., Kirkby, J.,
935 Seinfeld, J. H., El-Haddad, I., Flagan, R. C. and Donahue, N. M.: Rapid growth of new atmospheric particles by
936 nitric acid and ammonia condensation, Nature, doi:10.1038/s41586-020-2270-4, 2020.

937 Washenfelder, R. A., Langford, A. O., Fuchs, H. and Brown, S. S.: Measurement of glyoxal using an incoherent
938 broadband cavity enhanced absorption spectrometer, Atmos. Chem. Phys., doi:10.5194/acp-8-7779-2008, 2008.

939

940

941 **Table 1: Cluster formation enthalpies of different species with bromide ions.** The cluster geometries are optimized
942 at the ωB97X-D/aug-cc-pVTZ-PP level at 298.15 K. The enthalpies are calculated at the DLPNO-CCSD(T)/def2-
943 QZVPP//ωB97xD/aug-cc-pVTZ-PP level at 298.15 K.

Cluster formation pathway	Formation enthalpies (kcal mol^{-1})
$Cl_2 + Br^- \rightarrow Cl_2 \cdot Br^-$	-22.3
$OIO + Br^- \rightarrow OIO \cdot Br^-$	-23.2
$IO + Br^- \rightarrow IO \cdot Br^-$	-24.5
$HIO_3 + Br^- \rightarrow HIO_3 \cdot Br^-$	-26.6
$HOI + Br^- \rightarrow HOI \cdot Br^-$	-26.9
$HIO_2 + Br^- \rightarrow HIO_2 \cdot Br^-$	-29.2
$I_2 + Br^- \rightarrow I_2 \cdot Br^-$	-33.7
$ICl + Br^- \rightarrow ICl \cdot Br^-$	-33.8
$IBr + Br^- \rightarrow IBr \cdot Br^-$	-36.7
$H_2SO_4 + Br^- \rightarrow H_2SO_4 \cdot Br^-$	-41.1
$I_2O_4 + Br^- \rightarrow I_2O_4 \cdot Br^-$	-42.6
$I_2O_5 + Br^- \rightarrow I_2O_5 \cdot Br^-$	-53.2

944

945 **Table 2: Fragmentation reaction enthalpies of different species with bromide ions.** The cluster geometries are
946 optimized at the ωB97X-D/aug-cc-pVTZ-PP level at 298.15 K. The enthalpies are calculated at the DLPNO-
947 CCSD(T)/def2-QZVPP//ωB97xD/aug-cc-pVTZ-PP level at 298.15 K.

Cluster fragmentation pathway	Fragmentation enthalpies (kcal mol^{-1})
$Cl_2 \cdot Br^- \rightarrow Cl_2 + Br^-$	22.3
$Cl_2 \cdot Br^- \rightarrow BrCl + Cl^-$	22.3
$HIO_3 \cdot Br^- \rightarrow HIO_3 + Br^-$	26.6
$HIO_3 \cdot Br^- \rightarrow IO_3^- + HBr$	20.8
$HIO_3 \cdot Br^- \rightarrow IO_2^- + HOBr$	52.0
$HOI \cdot Br^- \rightarrow HOI + Br^-$	26.9
$HOI \cdot Br^- \rightarrow IO^- + HBr$	57.7
$HOI \cdot Br^- \rightarrow I^- + HOBr$	31.3
$HIO_2 \cdot Br^- \rightarrow HIO_2 + Br^-$	29.2
$HIO_2 \cdot Br^- \rightarrow IO_2^- + HBr$	43.8
$HIO_2 \cdot Br^- \rightarrow IO^- + HOBr$	42.2
$I_2 \cdot Br^- \rightarrow I_2 + Br^-$	33.7

$I_2 \cdot Br^- \rightarrow IBr + I^-$	33.8
$ICl \cdot Br^- \rightarrow ICl + Br^-$	33.8
$ICl \cdot Br^- \rightarrow IBr + Cl^-$	39.8
$ICl \cdot Br^- \rightarrow BrCl + I^-$	42.0
$IBr \cdot Br^- \rightarrow IBr + Br^-$	36.7
$IBr \cdot Br^- \rightarrow Br_2 + I^-$	39.4
$H_2SO_4 \cdot Br^- \rightarrow H_2SO_4 + Br^-$	41.1
$H_2SO_4 \cdot Br^- \rightarrow HSO_4^- + HBr$	27.9

948

949 **Table 3: Calibration coefficients for selected species.**

Species	Calibration coefficient (molec cm^{-3} cps cps^{-1})	Detection limit (molec cm^{-3})
[a] I_2	[a] 2.7×10^{10}	3.8×10^5
[a] H_2SO_4	4.1×10^{10}	2.0×10^5
[b] I_2	[b] 6.3×10^{10}	8.8×10^5
[b] Cl_2	[b] 3.5×10^{11}	n/a
[b] HOI	[b] 3.3×10^{11}	5.8×10^6
~~H_2SO_4~~	[a] ~~4.1×10^{10}~~	
[c] HIO_3	4.1×10^{10}	1.2×10^5

950 [a] Inter-method calibrations

951 [b] Offline calibrations

952 [c] Derived from dissociation enthalpies